DEPARTMENT OF PHYSICS, UNIVERSITY OF JYVÄSKYLÄ
RESEARCH REPORT No. 5/1998

SIMULATIONS OF FLUID FLOW IN POROUS MEDIA BY LATTICE-GAS AND LATTICE-BOLTZMANN METHODS

BY
ANTTI KOPONEN

Academic Dissertation
for the Degree of
Doctor of Philosophy

Jyväskylä, Finland
June 1998

URN:ISBN:978-951-39-9689-5
ISBN 978-951-39-9689-5 (PDF)
ISSN 0075-465X

Jyväskylän yliopisto, 2023

ISBN 951-39-0219-6
ISSN 0075-465X

DEPARTMENT OF PHYSICS, UNIVERSITY OF JYVÄSKYLÄ
RESEARCH REPORT No. 5/1998

SIMULATIONS OF FLUID FLOW IN POROUS MEDIA BY LATTICE-GAS AND LATTICE-BOLTZMANN METHODS

BY
ANTTI KOPONEN

Academic Dissertation
for the Degree of
Doctor of Philosophy

To be presented, by permission of the
Faculty of Mathematics and Natural Sciences
of the University of Jyväskylä,
for public examination in Auditorium FYS-1 of the
University of Jyväskylä on June 8, 1998,
at 12 o'clock noon

Jyväskylä, Finland
June 1998

Preface

This work has been carried out during the years 1994–1998 at the Department of Physics in the University of Jyväskylä.

First of all I would like to thank my supervisors Jussi Timonen and Markku Kataja for competent guidance. Working with them has been instructive and enjoyable. Warm thanks to my roommate Markku Kellomäki for nice partnership and for helping me with many practical problems. Special thanks to Drona Kandhai for excellent and productive co-operation. Other collaborators and colleagues who have contributed to my work in various ways are also highly acknowledged.

I would like to thank the Department of Physics for providing excellent working conditions and for its most friendly and stimulating athmosphere. The financial support from the Academy of Finland and the University of Jyväskylä are also gratefully acknowledged.

Finally, I would like to thank my family, my friends, and Soile for their support and encouragement.

Jyväskylä, June 1998

Antti Koponen

Abstract

Lattice-gas and lattice-Boltzmann methods can provide promising alternative approaches to traditional computational fluid dynamics. The geometric versatility of these methods makes them very attractive for simulating many complex systems, such as fluid flow in irregular geometries. Also, the inherent spatial locality of their updating rules makes these methods ideal for parallel computing. In this work, the basic ideas of these methods are first introduced. Then, many practical problems, such as boundary conditions, discretization errors, simulation time, and parallelization, are discussed, and a new efficient relaxation method, the Iterative Momentum Relaxation (IMR) method, is introduced. It is also shown that, with the Orthogonal Recursive Bisection (ORB) method, the performance of a parallel lattice-Boltzmann code can be significantly improved. Finally, several results of lattice-gas and lattice-Boltzmann simulations of single-fluid flow in 2D and 3D porous media are discussed. Simulation results for the tortuosity, effective porosity and permeability of a 2D random porous medium are reported. A modified Kozeny-Carman law is suggested, which includes the concept of effective porosity. This law is found to fit well the simulated 2D permeabilities. The results for fluid flow through large 3D random fibre webs are also presented. The simulated permeabilities of these webs are found to be in good agreement with experimental data. The simulations also confirm that, for this kind of materials, permeability depends exponentially on porosity over a large porosity range.

Contents

Chapter 1

Introduction

1.1 Computational fluid dynamics

The two basic hydrodynamic equations that describe the motion of fluid are the continuity equation

$$\partial_t \rho + \nabla \cdot (\rho \mathbf{u}) = 0, \tag{1.1}$$

which expresses the conservation of mass, and the Navier-Stokes equation

$$\partial_t (\rho \mathbf{u}) + \nabla \cdot (\rho \mathbf{u}\mathbf{u}) = -\nabla p + \nabla \cdot \tau + \mathbf{q}, \tag{1.2}$$

which expresses the conservation of momentum [1]. Here ρ is the fluid density, $\mathbf{u}$ is the fluid velocity, p is the hydrostatic pressure, τ is the fluid stress tensor, and $\mathbf{q}$ is an extra interaction term that can include *e.g.* the effect of gravity on the fluid. If the fluid is incompressible and Newtonian (in Newtonian fluid stresses are directly proportial to the velocity gradients $\partial_i u_j$), Eq. (1.2) can be expressed in the form [1]

$$\partial_t (\rho \mathbf{u}) + \nabla \cdot (\rho \mathbf{u}\mathbf{u}) = -\nabla p + \mu \nabla^2 \mathbf{u} + \mathbf{q}, \tag{1.3}$$

where μ is the dynamic viscosity of the fluid. This equation is often written in the form

$$\partial_t \mathbf{u} + (\mathbf{u} \cdot \nabla)\mathbf{u} = -\frac{}{\rho}\nabla p + \nu \nabla^2 \mathbf{u} + \mathbf{q}', \tag{1.4}$$

where $\nu = \mu/\rho$ is the kinematic viscosity of the fluid.

Eqs. (1.1) and (1.3) consist in their most general form of four highly nonlinear coupled partial differential equations which allow complete analytical solution in only some special cases. Sometimes these equations can

be simplified. In the case of stationary creeping flow, *e.g.*, the left-hand side of the Navier-Stokes equation vanishes and the Stokes equation,

$$\nabla p = \mu \nabla^2 \mathbf{u}, \tag{1.5}$$

is obtained. On the other hand, if viscous effects are small, the Euler equation,

$$\partial_t \mathbf{u} + (\mathbf{u} \cdot \nabla)\mathbf{u} = -\frac{1}{\rho}\nabla p, \tag{1.6}$$

is obtained. (In both these cases the effect of external forces has been omitted.) However, even after simplifications the equations still remain difficult to solve.

For a long time, the only practical way of studying many fluid-dynamical problems was to actually build the systems or models of them, and then study their behaviour *e.g.* in wind tunnels [2]. With sophisticated diagnostics, gross properties of the flow, such as drag and lift, could then be measured. With considerably more effort, information about the spatial dependence of some thermodynamic properties like pressure could also be acquired.

With the advent of computers it first seemed possible to gradually get rid of the cumbersome necessities of wind-tunnel experimentation by solving the equations of fluid flow numerically. Simulating fluid flow on computers, *i.e.* computational fluid dynamics (CFD), has indeed proved an invaluable tool for studing many fluid-flow phenomena. However, the difficulties with grid generation, problems with numerical stability, and the computational requirements for memory capacity and computational speed, have often restricted the use of this approach. Especially in the high Reynolds-number regime, the direct full-scale simulation of turbulence seems to stay beyond our computational capabilities in the foreseeable future. Many practical problems with small Reynolds numbers, like fluid flow in porous media or multiphase flows, have also proved to be suprisingly difficult to solve. Grid generation, *e.g.*, can be an extremerely difficult task in such systems, as they often include very complex boundaries, which may even be time dependent. Significant improvements in computational models and considerable increase in computational power are thus necessary if computational fluid dynamics is really to become a general-purpose alternative to experimental studies.

1.2 The lattice-gas model

Numerical solution of the Navier-Stokes equation has traditionally concentrated on directly finding a mathematical solution for the differential continuum equations governing the fluid flow. In principle, it would be possible to solve any fluid-flow problem on microscopic (atomic) level with direct molecular-dynamical simulations. Such simulations are computationally very intensive, and at present something like 10^9 particles can be used. This is a very small amount when compared with the number of particles found in real fluid-dynamical systems. It is thus clear that practical fluid-flow problems cannot be solved with this approach.

However, many dynamical systems can be modelled with radically simplified models. This fact has been utilized, *e.g.*, in the famous Ising models for magnetic materials, and since 1950's in various cellular-automaton models for biological and physical systems. The success of these models encouraged people to develop discrete models for fluids, too. For a long time these models were qualitatively incorrect. However, in 1986 it was realised that fluid could be simulated with very simple discrete models if the simulation lattice was chosen in a correct way [3]. This discovery was the starting point for the lattice-gas [4, 5, 6] and later lattice-Boltzmann methods [6, 7].

Space, time and particle velocities are all discrete in the lattice-gas model. Fluid is modelled with identical particles which move in a discrete lattice interacting with each other only at the lattice nodes. If the particle collisions satisfy mass and momentum conservation, and if the simulation lattice fulfils certain symmetry requirements, the lattice-gas automaton will develop macroscopic dynamics which is very close to incompressible Navier-Stokes behaviour.

The boolean and local nature of the lattice-gas model gives several advantages. Since the updating rules are strictly local and very simple, the introduction of complex boundaries is a simple matter, and the model is thus quite insensitive to the geometry of the simulated system. Due to its microscopic nature, the model is also easily extended to deal with a number of phenomena that are more complicated than incompressible single-phase flow. Because particles can be represented by single bits in the computer memory, the memory requirements are relatively small, and because there are no rounding off errors involved in bit manipulations, unconditional numerical stability is guaranteed. The computations are also inherently parallel being ideal for massively parallel computers.

The early lattice gases had also some drawbacks [6, 7]: The model had

a lot of statistical noise due to boolean computation, and a large number of lattice points (or a large number of iteration steps) were necessary in order to perform realistic fluid-dynamical simulations. Due to the large number of post-collision states, the collision operator had an exponential complexity with respect to the dimensions of the lattice. Furthermore, the dynamics of the fluid was not Galilean invariant, and fluid pressure was velocity dependent. The dependence of viscosity on the collision rules also restricted the model to rather limited range of Reynolds numbers.

Later many sophistications have helped to get rid of most of the problems mentioned above (see *e.g.* Refs. [2, 6, 8, 9]), and the lattice-gas method is a viable alternative to computational fluid dynamics.

1.3 The lattice-Boltzmann model

The early deficiencies of the lattice-gas models inspired the formulation of the lattice-Boltzmann models. The so-called non linear lattice-Boltzmann model was the first of them [10]. The idea behind this model was to track a population of particles instead of a single particle, a reasonable modification justified by the Boltzmann molecular-chaos assumption from kinetic theory. This mean-value representation of particles eliminated the problem of statistical noise. In order to break down the exponential complexity of the collision operator and to eliminate the need of using lattice-gas collisions in the lattice-Boltzmann models, a linearized version (the so-called enhanced-collision method) was then developed [11]. In the next step Maxwellian velocity distribution of the particles and inclusion of rest particles in the model led to Galilean invariant macroscopic behaviour [12]. The latest major modification to date is the lattice-BGK (Bhatnagar-Gross-Krook) model, where the collision operator is based on single-time relaxation to the local equilibrium distribution [13]. This is the simplest model in the hierarchy of lattice-Boltzmann methods, and it is regularly used in practical lattice-Boltzmann simulations.

The main drawback of the lattice-Boltzmann model when compared to the lattice-gas model is its lack of unconditional numerical stability. Also, the statistical noise in lattice gases can sometimes be useful for including autocorrelations in the model.

Both models have proved to be promising alternative approaches to traditional computational fluid dynamics. These methods have been particularly succesfull in modelling such singularly complex fluid-flow phenomena

as multiphase flows [5, 14], suspension flows [15], and flows in complex geometries [14], which all have been very difficult to simulate with conventional methods.

1.4 Fluid flow in porous media

Fluid flow in porous media plays an important role in a wide variety of technical and environmental processes such as oil recovery, paper making, and spread of hazardous wastes in soils. The most important law governing single-fluid flows is Darcy's law [16, 17]

$$\mathbf{q} = \frac{k}{\mu}\nabla p, \tag{1.7}$$

where $\mathbf{q}$ is the volumetric fluid flow through the medium, μ is the dynamic viscosity of the fluid, p is the fluid pressure, and k is the permeability coefficient that is a measure of the fluid conductivity of the porous medium. Equation (1.7) has been found to work very well with a wide variety of natural porous media when the fluid velocity is small.

In theoretical and experimental work on fluid flow in porous media it is typically attempted to find functional correlations between the permeability and some other macroscopic properties of the porous medium. Among the most important of such properties are the porosity ϕ and the specific surface area S, which give the ratios of the total void volume and the total interstitial surface area to the bulk volume, respectively. Another useful characteristics of porous media is the tortuosity τ, which has been introduced to account for the complexity of the actual microscopic flow paths through the substance. The experimental methods that have been used to find these functional correlations vary from rather straightforward measurements [18, 19, 20] to more sophisticated approaches, which utilize *e.g.* mercury porosimetry, electrical conductivity, nuclear magnetic resonance, or acoustic properties of the medium [21]. Theoretical methods typically rely on analytical models based on simplified pore geometries, which allow solution of the microscopic flow patterns [22], or on more advanced methods that statistically take into account the structural complexity of the medium [22, 23].

The two basic equations that are usually used to describe the permeable behaviour of porous media, are Kozeny's law [17, 22, 24, 25]

$$k = \frac{\phi^3}{cS^2}, \tag{1.8}$$

and Kozeny-Carman law

$$k = \frac{\phi^3}{c\tau^2 S^2}, \tag{1.9}$$

where c is so-called "Kozeny constant", which in most cases depends on the geometry of the porous sample. Equations. (1.8) and (1.9) can be derived analytically for many simplified models, and they give the qualitative permeable behaviour of many natural porous media rather well. However, the correctness of these two equations is generally not very good (*i.e.* the dependence of c on ϕ is often very strong).

The phenomena involved in fluid flow in porous media are very complex, and despite the numerous experimental and theoretical studies, permeable characteristics of porous media is still poorly understood. Various sophistications to Eqs. (1.8) and (1.9) have been suggested [22, 23, 26], but a general formula for permeability is still lacking. Experimental work is thus almost always obligatory in determination of permeability.

Numerical simulations are increasingly used in the study of complicated physical phenomena. They are often very useful in connecting theory with experiment, and they can also be used to reduce the number of experiments. Although realistic simulations of fluid flow in complex geometries, like in porous medium, are exceptionally demanding in terms of computing power, the new techniques based on massively parallel computers, increased single processor capabilities, and the recent introduction of new simulation models (the lattice-gas and lattice-Boltzmann methods in particular) have finally made them possible [I, 6, 14, 27].

1.5 Outline of the text

The first objective of this thesis is to give a rather detailed description of the lattice-gas and lattice-Boltzmann methods from both a theoretical and a practical point of view. The second objective is to present results from our lattice-gas and lattice-Boltzmann simulations of fluid flow in porous medium.

In Chapters 2 and 3 we introduce the lattice-gas and lattice-Boltzmann methods, and we show how the continuity equation Eq. (1.1) and Navier-Stokes equation Eq. (1.3) are obtained from their microdynamics. Then, in Chapter 4, we discuss several practical problems related to these methods, such as discretization errors, finite-size effects, driving forces, and parallelization. We also present several results from our lattice-gas and lattice-Boltzmann benchmark studies. In Chapter 5 we first discuss the concept

of fluid flow in porous medium in general, and briefly review the previous lattice-gas and lattice-Boltzmann studies on this topic. Next we discuss the basic physics of fluid flow in porous medium. Here the concepts of tortuosity and effective porosity will get special attention. Then we present our simulation results for the tortuosity, effective porosity, and permeability of a 2D random porous medium, and compare the simulated permeabilities with various theoretical predictions. Finally, we present results for fluid flow in large 3D random fibre webs, and show that these results compare very well with experimental data.

Chapter 2

Lattice-gas hydrodynamics

In this chapter we introduce the lattice-gas model and show how the macroscopic Navier-Stokes equation is obtained from its microdynamics. The objective of this chapter is to clarify the assumptions on which this model is based, and to discuss the physical features needed to construct lattice models that can yield the true fluid dynamics. We do not go very deeply into the technical details, as they can be found in the literature.

For lattice-gas models the classical paper is Ref. [4]. Other useful works are Refs. [2, 5, 6, 28, 29]. Our derivation of the Navier-Stokes equation is based mainly on Ref. [29], in which for both the lattice-gas and lattice-Boltzmann model an excellent derivation of the Navier-Stokes equation is given.

2.1 The lattice-gas model

The basic properties of most (single-speed) lattice-gas models are:

- The fluid is described with discrete identical fluid particles.
- The particles move in a discrete lattice. They reside only at the lattice nodes.
- Time is discrete.
- The speed of the particles is such that, during each time-step, they move from a lattice node to one of its nearest neighbours.
- An exclusion principle is obeyed: at each lattice node particles are not allowed to have identical velocities.

- When the particles meet at lattice nodes they can interact subject to mass and momentum conservation. This interaction, collision, may lead to reshuffling of particle velocities.

The discrete nature of lattice gas is quite different from real fluid, where particles are free to move in any direction and have a continuous spectrum of speeds. One should see the lattice gas as a computational tool for doing macroscopic fluid dynamics in an fictitious discrete world, which has the same kind of macroscopic behaviour as real fluids. Instead, the lattice-gas model *is not* a discrete description of the behaviour of atoms, molecules or even small fluid particles in real fluids.

Any lattice-gas model fulfilling the above mentioned basic properties does not necessarily give correct quantitative hydrodynamics. The discreteness of the model may lead to several unphysical artefacts such as

- Unisotropic stress tensor.
- Lack of Galilean invariance in the momentum equation.
- Velocity-dependent pressure.
- Unphysical conserved quantities (spurious invariants).

The anisotropy of the stress tensor can be removed with an appropriate choice of the lattice. For this reason the triangular lattice must be used in 2D single-speed models. In three dimensions, no lattice exists that would yield isotropy. For this reason a 3D projection of the 4D face-centered hypercubic (fchc) lattice is regularly used. The next two artefacts cannot generally be removed without introducing conservation of energy to the model [2]. The spurious invariants are caused by the discrete nature of the lattice, and are always present in lattice-gas models [30, 31].

Despite all these artefacts, very simple lattice-gas models can be used for quantitative hydrodynamics if the restrictions of the model are kept in mind.

2.2 FHP models

The so-called HPP model [29, 32, 33] is the simplest way of doing two-dimensional lattice-gas hydrodynamics. This model uses a square lattice, and it is too simple to yield quantitatively correct hydrodynamic behaviour.

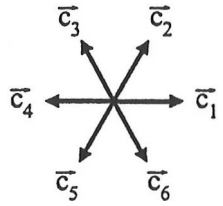

Figure 2.1: The directions $\mathbf{c}_i$ of particle velocities. (Taken from Ref. [29].)

The dynamics of the model is unisotropic, and it also contains several spurious invariants. (In a periodic lattice *e.g.* the fluid momentum is conserved along each horizontal or vertical line.)

In 1986, Frisch, Hasslacher, and Pomeau proved that the unphysical artefacts of the HPP model could be removed by using a triangular lattice [3]. (The six possible directions of particle motion $\mathbf{c}_i$ (i=1,...,6) in this lattice are shown in Fig. 2.1.) The simplest of these so-called FHP models, the FHP-I model, includes only two-particle and three-particle collisions (see Fig. 2.2). This model has no rest particles, and at most six particles can reside at each lattice node.

2.3 From lattice-gas microdynamics to macroscopic hydrodynamics

Let us denote the lattice time step by η, and the lattice spacing by λ. The six possible particle velocities are then

$$\mathbf{v}_i = \frac{\lambda}{\eta}\mathbf{c}_i. \tag{2.1}$$

We also define the particle occupation number $n_i(\mathbf{r}, t)$, which tells if there is a particle at site $\mathbf{r}$ at time t going in the $\mathbf{c}_i$-direction. (It is either 0 or 1.) The evolution equation for n_i is

$$n_i(\mathbf{r} + \lambda\mathbf{c}_i, t + \eta) = n_i(\mathbf{r}, t) + \Omega_i(\mathbf{r}, t), \tag{2.2}$$

where $\Omega_i(\mathbf{r}, t)$ is a model-dependent collision term that acts as a sink or source for type i particles. The actual form of this term is not interesting at the moment as the detailed nature of the microscopic interactions does not

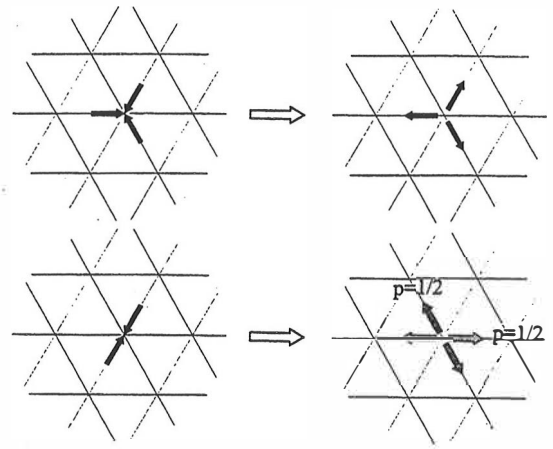

Figure 2.2: In the FHP-I model particles move in a triangular lattice, and there are only two-particle and three-particle collisions. A two-particle collision has two possible outcomes that both occur with probability 1/2. (Taken from Ref. [29].)

affect the form of the momentum equation. Their effect is only seen in the values of physical coefficients (such as viscosity) appearing in this equation.

In kinetic theory the physical quantities of interest such as density ρ, velocity $\mathbf{u}$, and momentum tensor Π, are obtained from velocity moments of the velocity distribution function [15, 34]. In lattice-gas models they are obtained from the discrete velocity moments of the ensemble averages $N_i(\mathbf{r},t) = \langle n_i(\mathbf{r},t)\rangle$ of the occupation numbers ($N_i(\mathbf{r},t)$ gives the probability of finding at $(\mathbf{r},t)$ a particle going in the $\mathbf{c}_i$ direction):

$$\rho(\mathbf{r},t) = \sum_{i=1}^{6} N_i(\mathbf{r},t), \tag{2.3}$$

$$\rho(\mathbf{r},t)\mathbf{u}(\mathbf{r},t) = \sum_{i=1}^{6} \mathbf{v}_i N_i(\mathbf{r},t), \tag{2.4}$$

and

$$\Pi_{\alpha\beta}(\mathbf{r},t) = \sum_{i=1}^{6} v_{i\alpha} v_{i\beta} N_i(\mathbf{r},t). \tag{2.5}$$

Here the greek letters α and β label the two spatial components of the velocity vectors.

The Boltzmann equation gives in kinetic theory the dynamics of the velocity distribution function [34]. Taking an ensemble average over Eq. (2.2), we get a corresponding equation for N_i:

$$N_i(\mathbf{r} + \lambda \mathbf{c}_i, t + \eta) = N_i(\mathbf{r}, t) + \langle \Omega_i(\mathbf{r}, t) \rangle. \tag{2.6}$$

Equation (2.6) is quite difficult to solve, and several approximations and simplifications are needed. We will here use the Chapman-Enskog expansion, which is commonly used in statistical mechanics for deriving macroscopic laws for relevant physical quantities when the Boltzmann equation is known [29].

We assume that the lattice spacing λ and timestep η are small compared to the characteristic system length L and time scale T. Then N_i are smooth functions of the time and space coordinates, and Eq. (2.6) can be Taylor-expanded up to second order to give

$$\begin{aligned} \eta \partial_t N_i + \lambda (\mathbf{c}_i \cdot \nabla) N_i &+ \frac{\eta^2}{2} \partial_t^2 N_i + \frac{\lambda^2}{2} (\mathbf{c}_i \cdot \nabla)^2 N_i + \\ \lambda \eta (\mathbf{c}_i \cdot \nabla) \partial_t N_i &= \langle \Omega_i \rangle. \end{aligned} \tag{2.7}$$

The first step in the Chapman-Enskog expansion is to write down a pertubation expansion of N_i:

$$N_i = N_i^{(0)} + \epsilon N_i^{(1)} + \epsilon^2 N_i^{(2)} + \ldots, \tag{2.8}$$

where ϵ is a small parameter. In order to determine the $N_i^{(l)}$ uniquely and consistently, we choose them in such a way that the macroscopic quantities ρ and $\rho \mathbf{u}$ are entirely given by the zeroth order term of the expansion [29]:

$$\rho = \sum_{i=1}^{6} N_i^{(0)} \tag{2.9}$$

$$\rho \mathbf{u} = \sum_{i=1}^{6} \mathbf{v}_i N_i^{(0)}. \tag{2.10}$$

It follows therefore that

$$\sum_{i=1}^{6} N_i^{(l)} = 0, \quad \sum_{i=1}^{6} \mathbf{v}_i N_i^{(l)} = 0, \quad \text{for} \quad l \geq 1. \tag{2.11}$$

Now, *we do not know how λ and η are related in the continuum limit.* From a physical ground, we expect to observe phenomena of several time scales. For instance, the ratio λ/η is the velocity of particles and should not vanish in the continuum limit. In addition, dissipative forces (like viscosity) will be present too, and with a coefficient of order λ^2/η [4, 29]. So, there are phenomena of several time scales included, and no single limiting relation between λ and η exists. For this reason we consider two macroscopic time scales T_1 and T_2 satisfying

$$\frac{\eta}{T_1} = \mathrm{O}(\epsilon), \quad \frac{\eta}{T_2} = \mathrm{O}(\epsilon^2), \tag{2.12}$$

and one macroscopic length scale satisfying

$$\frac{\lambda}{L_1} = \mathrm{O}(\epsilon). \tag{2.13}$$

Two time variables t_1 and t_2 are now defined such that

$$t = \frac{t_1}{\epsilon} + \frac{t_2}{\epsilon^2}. \tag{2.14}$$

Similarly, a macroscopic space variable $\mathbf{r}_1$ is introduced, related to $\mathbf{r}$ through $\mathbf{r} = \mathbf{r}_1/\epsilon$. The differentials ∂_t and ∂_α become now

$$\partial_t = \epsilon\partial_{t_1} + \epsilon^2\partial_{t_2} \tag{2.15}$$

and

$$\partial_\alpha = \epsilon\partial_{1\alpha}. \tag{2.16}$$

The next step is to identify the various orders of ϵ in Eq. (2.7). We do not yet know the exact form of the collision operator $\langle\Omega_i\rangle$, but we know that it must conserve mass and momentum. Collision operator $\langle\Omega_i\rangle$ thus must have the following general properties,

$$\sum_{i=1}^{6}\langle\Omega_i\rangle = 0, \qquad \sum_{i=1}^{6}\mathbf{v}_i\langle\Omega_i\rangle = 0. \tag{2.17}$$

Now, using Eqs. (2.8), (2.15), (2.16) and (2.17) to order ϵ^1, Eq. (2.7) can be expressed in the forms [29]:

$$\mathrm{O}(\epsilon): \qquad \partial_{t_1}\rho + \nabla_1\cdot(\rho\mathbf{u}) = 0 \tag{2.18}$$

and

$$O(\epsilon): \qquad \partial_{t_1}(\rho u_\alpha) + \partial_{1\beta}\Pi^{(0)}_{\alpha\beta} = 0, \tag{2.19}$$

where $\Pi^{(0)}$ is the zeroth order approximation of the momentum tensor Π. In the second order, Eq. (2.7) gives [29]

$$O(\epsilon^2): \quad \partial_{t_2}\rho = 0 \tag{2.20}$$

and

$$O(\epsilon^2): \quad \partial_{t_2}(\rho u_\alpha) + \partial_{1\beta}\left[\Pi^{(1)}_{\alpha\beta} + \frac{\eta}{2}(\partial_{t_1}\Pi^{(0)}_{\alpha\beta} + \partial_{1\gamma}S^{(0)}_{\alpha\beta\gamma})\right] = 0, \tag{2.21}$$

where S is a third order tensor defined as

$$S_{\alpha\beta\gamma} = \sum_{i=1}^{6} v_{i\alpha}v_{i\beta}v_{i\gamma}N_i. \tag{2.22}$$

Let us now take a closer look at Eqs. (2.18) – (2.21). Equation (2.18) resembles the continuity equation (1.1), while Eq. (2.20) shows that second order corrections to this equation are neglible. Combining (with the appropriate power of ϵ) both orders, we find that the lattice gas obeys the standard continuity equation,

$$\partial_t\rho + \nabla\cdot(\rho\mathbf{u}) = 0. \tag{2.23}$$

The first-order momentum equation Eq. (2.19) resembles the Euler equation. The viscous effects are introduced in the second-order correction (2.21) via the first-order term $\Pi^{(1)}$ of the momentum tensor. The momentum equation for the lattice gas, which is obtained by summing these two equations, is

$$\partial_t(\rho u_\alpha) + \partial_\beta\left[\Pi_{\alpha\beta} + \frac{\eta}{2}(\epsilon\partial_{t_1}\Pi^{(0)}_{\alpha\beta} + \partial_\gamma S^{(0)}_{\alpha\beta\gamma})\right] = 0. \tag{2.24}$$

The first two terms in Eq. (2.24) are the standard result of continuum kinetic theory (see *e.g.* [15, 34]). The last two terms, however, are unphysical. They follow from the discreteness of the model.

Notice that the momentum equation Eq. (2.24) is still very general, as we have not yet restricted ourselves to a given set of collision rules. (In fact, the actual structure of the lattice has not been used either.) The tensors Π and S in Eq. (2.24) must be expressed in terms of hydrodynamic variables ρ and $\mathbf{u}$, before we can see if the momentum equation of the lattice gas is really the standard Navier-Stokes equation. This derivation requires an

expression for N_i (the zeroth- and first-order terms $N_i^{(0)}$ and $N_i^{(1)}$ are found to be enough) as a function of ρ and $\mathbf{u}$. The explicit form of the collision operator is needed here.

In the FHP-I model only 2- and 3-particle collisions are included, and the collision operator Ω_i is

$$\Omega_i = -D_i + qD_{i-1} + (1-q)D_{i+1} - T_i + T_{i+3}. \tag{2.25}$$

Here D_j denotes a two-particle collision which removes a type j and a $j+3$ particle and produces two other ($j+1$ and $j+4$, or $j-1$ and $j+2$) particles. (Here index j runs periodically. For $j = 7$ *e.g.*, the value $j = 1$ is given.) Similarly, T_j denotes a three-particle collision between type $j, j+2$ and $j+4$ particles. Factor q is a boolean quantity which decides with equal probabilities, which of the two possible outcomes of the two-particle collision will be chosen (*i.e.* $\langle q \rangle = \frac{1}{2}$). The operators D_j and T_j are functions of the particle occupation numbers n_i. The two-body collision operator D_j, *e.g.*, is

$$D_j = n_j n_{j+3}(1-n_{j+1})(1-n_{j+2})(1-n_{j+4})(1-n_{j+5}). \tag{2.26}$$

Taking an ensemble average over Ω_i, we get

$$\begin{aligned} \langle \Omega_i \rangle \;=\; & -\langle D_i \rangle + \frac{1}{2}\langle D_{i-1} \rangle + \frac{1}{2}\langle D_{i+1} \rangle \\ & -\langle T_i \rangle + \langle T_{i+3} \rangle, \end{aligned} \tag{2.27}$$

where, *e.g.*,

$$\langle T_j \rangle \;=\; \langle n_j\, n_{j+2}\, n_{j+4}(1-n_{j+1})(1-n_{j+3})(1-n_{j+5}) \rangle. \tag{2.28}$$

The ensemble averages $\langle n_i n_j n_k \ldots \rangle$ are not easy to evaluate. To simplify the problem, the Boltzmann hypothesis of molecular chaos familiar from kinetic theory [34] is now used: we assume that collisions between the particles will destroy the particle-particle correlations so quickly that, in hydrodynamic phenomena, they are irrelevant. The Boltzmann hypothesis enables us to express the collision operators $\langle \Omega_i \rangle$ as products of $\langle n_j \rangle = N_j$. The three-body collision operator $\langle T_j \rangle$, *e.g.*, can be written in the form

$$\langle T_j \rangle = N_j\, N_{j+2}\, N_{j+4}(1-N_{j+1})(1-N_{j+3})(1-N_{j+5}). \tag{2.29}$$

The solution of Eq. (2.7) becomes now much easier, although tedious analysis is still needed. We shall first Taylor-expand the collision operator

$\Omega_i(N)$ (remember that $N_i = N_i^{(0)} + \epsilon N_i^{(1)} + \dots$). We find

$$\Omega_i(N) = \Omega_i(N^{(0)}) + \epsilon \sum_{j=1}^{6} \left(\frac{\partial \Omega_i(N^{(0)})}{\partial N_j} \right) N_j^{(1)} + \mathrm{O}(\epsilon^2). \tag{2.30}$$

The collision operator must be of order ϵ^1 at least [29], but the right hand side of Eq. (2.30) has a contribution of order ϵ^0. We thus get in the zeroth order

$$\mathrm{O}(\epsilon^0): \qquad \Omega_i(N^{(0)}) = 0. \tag{2.31}$$

This equation is used to determine $N_i^{(0)}$. The solutions $N_i^{(0)}$ make the collision term vanish, and for this reason they are known as the *local equilibrium solutions*. Physically they correspond to a situation where the rate of each type of collisions equilibrates. The first-order equation is obtained from Eqs. (2.7) and (2.30) [29]:

$$\mathrm{O}(\epsilon^1): \qquad \partial_{t_1} N_i^{(0)} + \partial_{1\alpha} v_{i\alpha} N_i^{(0)} = \frac{1}{\eta} \sum_{j=1}^{6} \left(\frac{\partial \Omega_i(N^{(0)})}{\partial N_j} \right) N_j^{(1)}. \tag{2.32}$$

When the equilibrium solutions $N_i^{(0)}$ have been found, the first-order terms $N_i^{(1)}$ can be obtained from Eq. (2.32).

The derivation of $N_i^{(0)}$ from Eq. (2.31) is quite complicated and will be omitted here. The final result is [29]

$$N_i^{(0)} = \frac{\rho}{6} + \frac{\rho}{3v} \mathbf{c}_i \cdot \mathbf{u} - \frac{1}{3} g(\rho) \rho \frac{u^2}{v^2} + \frac{2}{3} g(\rho) \rho c_{i\alpha} c_{i\beta} \frac{u_\alpha}{v} \frac{u_\beta}{v}, \tag{2.33}$$

where

$$g(\rho) = \frac{3 - \rho}{6 - \rho}. \tag{2.34}$$

Here the following tensor properties of the triangular lattice have been used:

$$\sum_{i=1}^{6} c_{i\alpha} = 0 \tag{2.35}$$

$$\sum_{i=1}^{6} c_{i\alpha} c_{i\beta} = 3\delta_{\alpha\beta}. \tag{2.36}$$

Two additional tensor properties are needed below, *i.e.*

$$\sum_{i=1}^{6} c_{i\alpha}c_{i\beta}c_{i\gamma} = 0 \tag{2.37}$$

$$\sum_{i=1}^{6} c_{i\alpha}c_{i\beta}c_{i\gamma}c_{i\delta} = \frac{3}{4}(\delta_{\alpha\beta}\delta_{\gamma\delta} + \delta_{\alpha\gamma}\delta_{\beta\delta} + \delta_{\alpha\delta}\delta_{\beta\gamma}). \tag{2.38}$$

Notice that all the tensors defined by Eqs. (2.35) – (2.38) are isotropic. For this reason the structure of the underlaying (triangular) lattice is not manifested in the macrodynamics of the system. This is an important reason for using the triangular lattice; in a square lattice the fourth-order tensor of Eq. (2.38) would be anisotropic. (In three dimensions no regular lattice exists that would make a single-speed model isotropic. Therefore a three-dimensional projection of the four dimensional face-centered hypercubic (fchc) lattice is usually used.)

The zeroth order term $\Pi^{(0)}_{\alpha\beta} = \sum_i v_{i\alpha}v_{i\beta}N_i^{(0)}$ can now be calculated by substituting $N_i^{(0)}$ into it. The result is [29]

$$\Pi^{(0)}_{\alpha\beta} = \sum_i v_{i\alpha}v_{i\beta}N_i^{(0)} \tag{2.39}$$

$$= \left(\frac{v^2}{2}\rho - \frac{\rho}{2}g(\rho)u^2\right)\delta_{\alpha\beta} + \rho g(\rho)u_\alpha u_\beta. \tag{2.40}$$

The corresponding result in kinetic theory is $\Pi^{(0)}_{\alpha\beta} = p\delta_{\alpha\beta} + \rho u_\alpha u_\beta$ [15, 34]. So, in the FHP-I model, pressure is given by

$$p = \frac{v^2}{2}\rho - \frac{\rho}{2}g(\rho)u^2. \tag{2.41}$$

The term $\frac{v^2}{2}\rho$ above corresponds to the ideal-gas equation of state at constant temperature. (In the FHP model temperature is not defined, and the equation for conservation of kinetic energy is identical to the mass-conservation equation.) The pressure of Eq. (2.41) also includes an unphysical velocity-dependent term $-\frac{\rho}{2}g(\rho)u^2$. However, this term is small in the incompressible limit, *i.e.* with small Mach numbers [5]. (The Mach number Ma is defined as Ma $= u/c_s$, where c_s is the speed of sound.)

Now, we can finally calculate the first-order momentum equation by substituting $\Pi^{(0)}_{\alpha\beta}$ into Eq. (2.19). We shall utilise here the standard approximation of hydrodynamics, that at low Mach numbers the fluid density is

non-constant only in the pressure term. We find [29] that

$$\rho\partial_{t_1}\mathbf{u} + g(\rho)\rho(\mathbf{u}\cdot\nabla_1)\mathbf{u} = -\nabla_1 p. \tag{2.42}$$

This expression differs from the standard Euler equation Eq. (1.6) in that the convection term includes a density dependent coefficient $g(\rho)$. Equation (2.42) is not therefore Galilean invariant.

The speed of sound c_s for the FHP-I model can be calculated from Eqs. (2.18) and (2.42) with the substitution $\rho = \rho_0 + \delta\rho$ and $\mathbf{u} = \delta\mathbf{u}$. Here $\delta\rho$ and $\delta\mathbf{u}$ are small fluctuations that propagate with the speed of sound c_s. We find [29] that

$$c_s^2 = \frac{v^2}{2}. \tag{2.43}$$

We can thus write

$$\Pi_{\alpha\beta}^{(0)} = c_s^2\rho\delta_{\alpha\beta} + \mathrm{O}(u^2). \tag{2.44}$$

The first-order non-equilibrium term $N_i^{(1)}$ can now be solved from Eq. (2.32) by substituting $N_i^{(0)}$ into it. The result is [29]

$$N_i^{(1)} = -\frac{2\eta}{3\rho(1-\rho/6)^3}(c_{i\alpha}c_{i\beta} - \frac{1}{2}\delta_{\alpha\beta})\partial_{1\beta}\rho u_\alpha. \tag{2.45}$$

(The terms higher than $\mathrm{O}(u)$ have been omitted.)

Finally, $N_i^{(0)}$ and $N_i^{(1)}$ can be substituted into Eq. (2.24) with the result [29] that

$$\begin{aligned}&\partial_t(\rho u_\alpha) + \partial_\beta(g(\rho)\rho u_\alpha u_\beta) = \\ &-\nabla p - \partial_\beta\left[\frac{\eta v^2}{2\rho(1-\rho/6)^3}(\delta_{\alpha\beta}\nabla\cdot(\rho\mathbf{u}) - (\partial_\alpha u_\beta + \partial_\beta u_\alpha))\right] \\ &-\frac{\eta v^2}{8}\nabla^2\rho u_\alpha,\end{aligned} \tag{2.46}$$

where pressure p is given by Eq. (2.41). In the limit of low Mach numbers we shall once again assume that density is nonconstant only in the pressure term. Then, the continuity equation Eq. (2.23) gives $\nabla\cdot(\rho\mathbf{u}) = 0$, and we find [29]

$$\partial_t\mathbf{u} + g(\rho)(\mathbf{u}\cdot\nabla)\mathbf{u} = -\frac{1}{\rho}\nabla p + \nu\nabla^2\mathbf{u}, \tag{2.47}$$

where

$$\nu = \eta v^2\left(\frac{1}{2\rho(1-\rho/6)^3} - \frac{1}{8}\right) \tag{2.48}$$

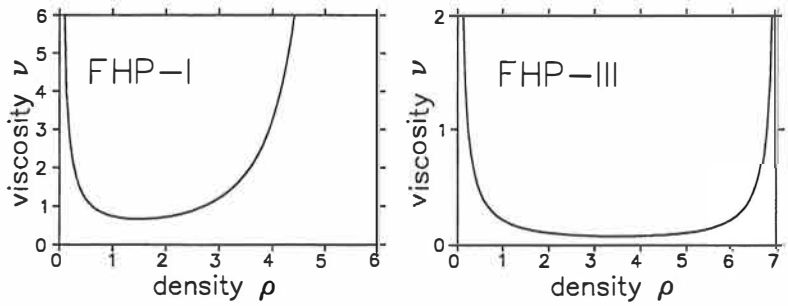

Figure 2.3: The density dependence of kinematic viscosity ν of the FHP-I and FHP-III models.

is the kinematic viscosity of the fluid. Here $\nu_{\rm coll} = \eta v^2/2\rho(1-\rho/6)^3$ is the *collision viscosity*, which is caused by the propagation and collisions of particles. The term $\nu_{\rm latt} = -\frac{1}{8}\eta v^2$ is the *lattice viscosity* which has no counterpart in real world. It originates from an unphysical term $\frac{\eta}{2}(\partial_{t_1}\Pi^{(0)}_{\alpha\beta} + \partial_\gamma S^{(0)}_{\alpha\beta\gamma})$ in Eq. (2.24), caused by the discreteness of the lattice. Fortunately, lattice viscosity appears in the macroscopic equation in such a way, that its only effect is a change in the total viscosity ν of the fluid.

We show in Fig. 2.3 the density dependence of viscosity. It is evident from this figure that increasing density from zero decreases viscosity up to $\rho = 1.5$, where viscosity reaches its minimum $\nu = 0.67$. (Here, and also below, lattice units are always used if the units are not specified.) This decrease is caused by an increase in the collision rate, which slows down the momentum diffusion in the system. The probability of two- and three-body collisions is small when density is high. For this reason viscosity increases after $\rho = 1.5$. (Notice that the derivation of Eq. (2.48) includes several simplifications. This expression is therefore not exact, and in practice the fluid viscosity is usually determined from simulations.)

The lattice viscosity is not the only unphysical artefact in Eq. (2.47). The $g(\rho)$ dependence of the convection term $g(\rho)(\mathbf{u}\cdot\nabla)\mathbf{u}$ leads to a model in which Galilean invariance is violated. One cannot get rid of this problem by tuning the density as $g(\rho)$ is always smaller than one (*cf.* Fig. 2.4). However, because density is approximately constant, the $g(\rho)$ factor can be absorbed in a renormalization of time by $\partial_{t_1} \to g(\rho)\partial'_t$, and the traditional Navier-Stokes equation is then obtained [5, 29]. One should also notice that, if we set $\rho = 3$, the convection term in Eq. (2.47) vanishes, and we get a Galilean invariant time-dependent Stokes equation.

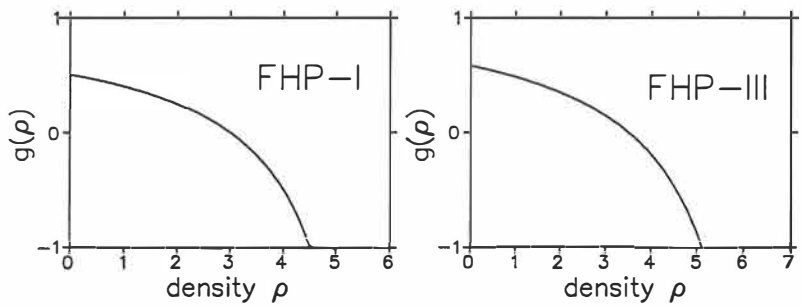

Figure 2.4: The density dependence of the $g(\rho)$ term of the FHP-I and FHP-III models.

2.4 The FHP-III model

In real gases viscosity is proportional to the mean free path λ_{mfp} of the atoms or molecules. This is true also for the lattice gases. In the FHP-I model [29]

$$\nu_{\text{coll}} = \frac{v}{12}\lambda_{\text{mfp}}, \tag{2.49}$$

where ν_{coll} is the collisional viscosity of the fluid, and λ_{mfp} is the mean free path of the lattice-gas particles. The minimum value of this mean free path $\lambda_{\text{mfp}} = 8.0$, is quite large, and the minimum viscosity is thus high in this model [29].

The mean free path can be decreased by increasing the collision probability. This can be done by increasing the number of different types of collisions and introducing rest particles into the model. In the FHP-III model one rest particle and all possible collisions are included [4]. (The collision table is shown in Fig. 2.5.) The dynamics of the system is once again given by Eq. (2.47), but with different expressions for $g(\rho)$ and $\nu(\rho)$ (see Figs. 2.3 and 2.4) [4]:

$$g(\rho) = \frac{7}{12}\frac{1-2\rho/7}{1-\rho/7} \tag{2.50}$$

and

$$\nu(\rho) = \eta v^2 \left(\frac{1}{4\rho(1-\rho/7)(1-8\rho(1-\rho/7)/49)} - \frac{1}{8} \right). \tag{2.51}$$

According to Eq. (2.51), the minimum viscosity of the FHP-III model is $\nu = 0.075$ (at $\rho = 3.5$). With this density $g(\rho)$ is zero, and the Stokes equation is obtained. The sound velocity is $c_s = \sqrt{\frac{3}{7}}$ [4]. At $\rho = 3.5$ the

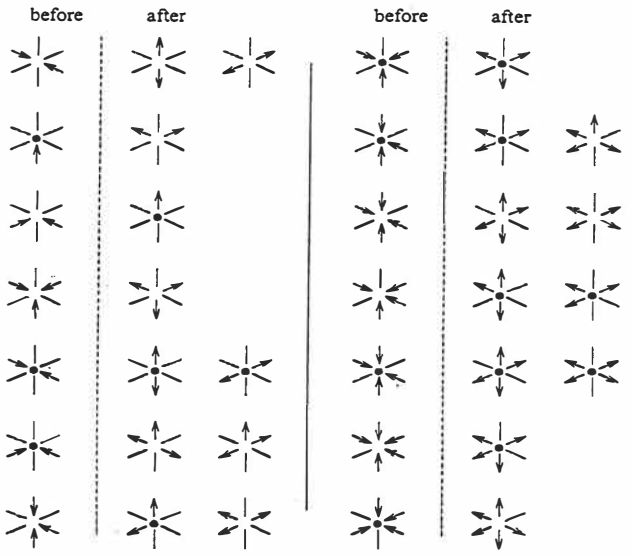

Figure 2.5: The collision table of the FHP-III model. 76 of the 128 different particle configurations lead to a collision. (Taken from Ref. [29].)

mean free path of the FHP-III model is $\lambda_{\mathrm{mfp}} = 2.9$. (Here one assumes that a particle of type i is involved in a collision if it disappears in the collision process. One gets $\lambda_{\mathrm{mfp}} = 1.7$ if the particles are regarded colliding although they would not disappear in the collision process.)

We have used the FHP-III model in our lattice-gas simulations.

2.5 Other lattice-gas models

There are no three-dimensional lattices that would yield a fourth-order isotropic tensor Eq. (2.38) in a one-speed model. For this reason 3D lattice-gas simulations are usually performed using a 3D projection of a one-speed model in the 4D face-centered hyper-cubic (fchc) lattice [2, 4, 5, 35]. This way one gets a 3D two-speed model with rest particles included. Although 3D lattice-gas simulations require much more computing power than 2D simulations, one can perform realistic simulations even on workstations [36, 37, 38].

The lattice-gas method can be modified in many ways. The various applications include miscible and immiscible multiphase flows [5, 38, 39, 40, 41], reactive systems [42, 43, 44], osmosis [45], suspension flows [46, 47],

thermodynamics [48, 49], and magnetohydrodynamics [50]. There are also multiparticle models (called integer lattice gases), where several particles can stay on each link [51, 52]. With these models most of the statistical noise is eliminated, Galilean invariance is obtained, and smaller viscosities can be reached.

Chapter 3

Lattice-Boltzmann hydrodynamics

In the previous chapter we derived the macroscopic equation for the dynamics of the lattice-gas model. In this chapter we introduce the lattice-Boltzmann model, in particular the lattice-BGK model, and show how the macroscopic Navier-Stokes dynamics is obtained from its microdynamics. Once again, we try to clarify the assumptions and the required physical features on which this model is based, without going too deep into the technical details.

For lattice-Boltzmann models the classical review paper is Ref. [7]. Other useful references are Refs. [6, 29]. Our derivation of the Navier-Stokes equation is based on Ref. [29], where for both the lattice-gas and lattice-Boltzmann models an excellent presentation of this derivation is given.

3.1 The lattice-Boltzmann method

The spontaneous statistical fluctuations inherent in lattice-gas models are important if long-time tails in the velocity autocorrelations are needed [29]. (They are important *e.g.* in reaction-diffusion models.) In many physical situations spontaneous fluctuations and many-particle correlations can be safely ignored, and one would like to eliminate the fluctuations *before* the simulation, not during it. This is exactly what is done in the lattice-Boltzmann method. Instead of simulating the dynamics of boolean-particle populations, the Boltzmann equation

$$f_i(\mathbf{r} + \lambda \mathbf{c}_i, t + \eta) = f_i(\mathbf{r}, t) + \Omega_i(\mathbf{r}, t) \tag{3.1}$$

is directly simulated. Here $f_i(\mathbf{r},t)$ gives the probability of having a particle of type i (or alternatively, the density of type i particles) at $(\mathbf{r},t)$, and $\Omega_i(\mathbf{r},t)$ is a collision operator. (With the symbol f_i instead of N_i for the particle populations, we want to emphasize that now we are directly dealing with real numbers instead of integers.) In contrast to Eq. (2.6), the collision operator can here be chosen quite freely, whereas in the lattice-gas model the collision operator was given purely by the possible particle-particle collisions. As we shall see, this freedom in choosing Ω_i gives several advantages: viscosity can be tuned easily and small viscosities can be obtained, the model can be made Galilean invariant, the velocity dependence of pressure can be removed, and the model can easily be expanded to 3D. The main drawback of the model, when compared to the lattice-gas model, is the lack of unconditional numerical stability.

We discussed in Chapter 1 the historical development of the lattice-Boltzmann models. Here we shall restrict ourselves to the latest model, the lattice-BGK model, where the collision operator is based on a single-time relaxation to the local equilibrium distribution [13]. This is the simplest model in the hierarchy of lattice-Boltzmann models, and it is regularly used in practical lattice-Boltzmann simulations. (Notice that the abbreviation BGK stands for Bhatnager, Gross and Krook who, in 1954, first considered a collision term with a single relaxation time [53].)

3.2 From lattice-Boltzmann microdynamics to macroscopic hydrodynamics

In the lattice-BGK model a single-time relaxation collision operator $\Omega_i = \frac{1}{\xi}(f_i^{(0)}(\mathbf{r},t) - f_i(\mathbf{r},t))$ is used, and the dynamics of the system is given by the equation

$$f_i(\mathbf{r}+\lambda\mathbf{c}_i, t+\eta) = f_i(\mathbf{r},t) + \frac{1}{\xi}(f_i^{(0)}(\mathbf{r},t) - f_i(\mathbf{r},t)). \tag{3.2}$$

Here, $f_i(\mathbf{r},t)$ is the particle density on the i-th link at $(\mathbf{r},t)$, $f_i^{(0)}$ is the equilibrium distribution, and ξ is a relaxation parameter. The equilibrium distribution $f_i^{(0)}$ is chosen to produce the required behaviour for the lattice-Boltzmann fluid. The first requirement for $f_i^{(0)}$ is of course mass and momentum conservation, but, with a suitable choice of $f_i^{(0)}$, many other properties can be obtained.

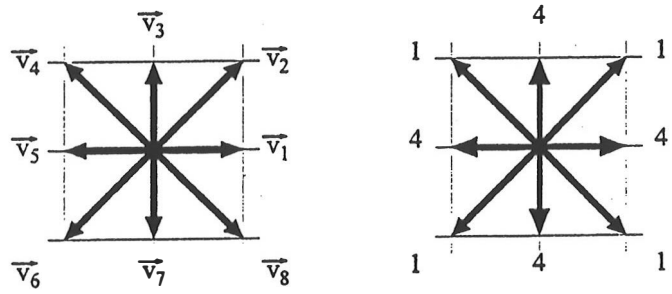

Figure 3.1: Left: The D2Q8 model has eight different particles and two different particle speeds. Right: The masses associated with the fluid particles. (Taken from Ref. [29].)

Notice that the type of relaxation of f_i towards $f_i^{(0)}$ depends on ξ [13]: if $\xi > 1$, relaxation is called subrelaxation (here f_i relaxes monotoneously towards $f_i^{(0)}$), if $\xi = 1$, the velocity distribution is immediately relaxed, and if $1/2 < \xi < 1$, relaxation is called over-relaxation (now f_i fluctuates around $f_i^{(0)}$). If ξ is equal or smaller than $1/2$, the algorithm is unstable.

In 2D lattice-Boltzmann models there are two basic choices for the simulation lattice. One could use once again the triangular lattice, but a square lattice is usually chosen due to its easier data structure. We shall study here the lattice-BGK D2Q8 model (here D denotes the dimensionality of the problem, and Q is the number of links per lattice point). In this model, the lattice points are connected to their nearest and next nearest neighbours (see Fig. 3.1). There are eight different particles, as rest particles are excluded, and two different particle speeds v_i: $1 \cdot \frac{\lambda}{\eta}$ and $\sqrt{2} \cdot \frac{\lambda}{\eta}$. (Here λ and η are the lattice spacing and the lattice time step, respectively.)

The solution to the equation Eq. (3.2) is once again obtained by using the Chapman-Enskog expansion

$$f_i = f_i^{(0)} + \epsilon f_i^{(1)} + \ldots, \tag{3.3}$$

where the equilibrium distribution $f_i^{(0)}$ is now *defined* as

$$\begin{aligned} f_i^{(0)} &= m_i F_i^{(0)} \\ &= m_i \left(a\rho + \frac{b}{v^2}\rho \mathbf{v}_i \cdot \mathbf{u} + \rho e \frac{u^2}{v^2} + \rho \frac{h}{v^4} (\mathbf{v}_i \cdot \mathbf{u})^2 \right). \end{aligned} \tag{3.4}$$

Here a, b, e, h are constants which are determined in such a way that the required fluid properties are obtained. (The general form of $F_i^{(0)}$ can also be seen in Eq. (2.33).) An isotropic model is obtained with the choice $m_i = 4$ for odd i, and $m_i = 1$ for even i (see Fig. 3.1). With this choice we get the following tensor properties [29]:

$$\sum_{i=1}^{8} m_i c_{i\alpha} = 0 \tag{3.5}$$

$$\sum_{i=1}^{8} m_i c_{i\alpha} c_{i\beta} = 12v^2 \delta_{\alpha\beta} \tag{3.6}$$

$$\sum_{i=1}^{8} m_i c_{i\alpha} c_{i\beta} c_{i\gamma} = 0 \tag{3.7}$$

$$\sum_{i=1}^{8} m_i c_{i\alpha} c_{i\beta} c_{i\gamma} c_{i\delta} = 4v^4 (\delta_{\alpha\beta}\delta_{\gamma\delta} + \delta_{\alpha\gamma}\delta_{\beta\delta} + \delta_{\alpha\delta}\delta_{\beta\gamma}) \tag{3.8}$$

(*cf.* Eqs. (2.35) – (2.38)).

The hydrodynamic variables ρ, $\mathbf{u}$ and Π can be expressed in the forms (*cf.* Eqs. (2.3) – (2.5))

$$\rho(\mathbf{r}, t) = \sum_{i=1}^{8} f_i(\mathbf{r}, t) = \sum_{i=1}^{8} m_i F_i(\mathbf{r}, t), \tag{3.9}$$

$$\rho(\mathbf{r}, t)\mathbf{u}(\mathbf{r}, t) = \sum_{i=1}^{8} \mathbf{v}_i f_i(\mathbf{r}, t) = \sum_{i=1}^{8} m_i \mathbf{v}_i F_i(\mathbf{r}, t), \tag{3.10}$$

and

$$\Pi_{\alpha\beta}(\mathbf{r}, t) = \sum_{i=1}^{8} v_{i\alpha} v_{i\beta} f_i(\mathbf{r}, t) = \sum_{i=1}^{8} m_i v_{i\alpha} v_{i\beta} F_i(\mathbf{r}, t). \tag{3.11}$$

We can now derive the constants a, b, e, h for the equilibrium distribution Eq. (3.4). The collision operator $\Omega_i \equiv m_i \omega_i$ must conserve mass and momentum, *i.e*

$$\sum_{i=1}^{8} m_i \omega_i = 0, \quad \sum_{i=1}^{8} m_i \mathbf{v}_i \omega_i = 0, \tag{3.12}$$

and we find [29]

$$a = \frac{1}{20}, \quad b = \frac{1}{12}, \quad 12h + 20e = 0. \tag{3.13}$$

For the zeroth-order momentum tensor $\Pi^{(0)}_{\alpha\beta}$ we find in a similar way [29]

$$\Pi^{(0)}_{\alpha\beta} = \sum_{i=1}^{8} m_i v_{i\alpha} v_{i\beta} F_i^{(0)} \tag{3.14}$$

$$= 12v^2 \left(a + (e + \frac{h}{3}) \frac{u^2}{v^2} \right) \rho \delta_{\alpha\beta} + 8h\rho u_\alpha u_\beta. \tag{3.15}$$

A Galilean invariant model is thus obtained if we choose

$$h = \frac{1}{8}, \tag{3.16}$$

which implies that

$$e = -\frac{3}{40}. \tag{3.17}$$

The expression for $\Pi^{(0)}_{\alpha\beta}$ now reads

$$\Pi^{(0)}_{\alpha\beta} = p\delta_{\alpha\beta} + \rho u_\alpha u_\beta, \tag{3.18}$$

where the hydrostatic pressure p is given by

$$p = 12v^2 \left(a + (e + \frac{h}{3}) \frac{u^2}{v^2} \right) \rho = \frac{3}{5} v^2 \left(1 - \frac{2}{3} \frac{u^2}{v^2} \right) \rho. \tag{3.19}$$

We can now write (*cf.* Eq. (2.44))

$$\Pi^{(0)}_{\alpha\beta} = c_s^2 \rho \delta_{\alpha\beta} + \mathrm{O}(u^2), \tag{3.20}$$

where the speed of sound c_s is

$$c_s^2 = \frac{3}{5} v^2. \tag{3.21}$$

(In Eq. (3.19), the pressure is velocity dependent. In the 9-link lattice-BGK model a rest particle is included, and this unphysical artefact is removed [54].)

The derivation of the Navier-Stokes equation is similar to the corresponding derivation for the lattice-gas model. The Boltzmann equation Eq. (3.2) is first Taylor-expanded, and then Eqs. (2.12), (2.13) and (3.12) are used. After some algebra one finds [29]

$$\partial_t \rho u_\alpha + \partial_\beta \left[\Pi_{\alpha\beta} + \frac{\eta}{2} (\epsilon \partial_{t_1} \Pi^{(0)}_{\alpha\beta} + \partial_\gamma S^{(0)}_{\alpha\beta\gamma}) \right] = 0, \tag{3.22}$$

where $S^{(0)}_{\alpha\beta\gamma}$ is defined as

$$S^{(0)}_{\alpha\beta\gamma} = \sum_{i=1}^{8} m_i v_{i\alpha} v_{i\beta} v_{i\gamma} F_i^{(0)}. \tag{3.23}$$

Equation (3.22) is identical with Eq. (2.24), because only the conservation properties of the collision operator, but not its actual form, have so far been used.

Now, we need to derive $S^{(0)}_{\alpha\beta\gamma}$, and the first-order term in the momentum tensor $\Pi_{\alpha\beta} = \Pi^{(0)}_{\alpha\beta} + \Pi^{(1)}_{\alpha\beta} + \ldots$ ($\Pi^{(0)}_{\alpha\beta}$ is already known). To this end the first-order correction to the velocity distribution F_i is needed. It can be derived from an equation similar to Eq. (2.32), namely [29]

$$\partial_{t_1} F_i^{(0)} + \partial_{1\alpha} v_{i\alpha} F_i^{(0)} = \frac{1}{\eta} \sum_{j=1}^{8} \left(\frac{\partial \omega_i(F^{(0)})}{\partial F_j} \right) F_j^{(1)}. \tag{3.24}$$

After some manipulations we find [29] that

$$F_i^{(1)} = -\eta\xi \frac{b}{v^2} (v_{i\alpha} v_{i\beta} - \frac{av^2}{b} \delta_{\alpha\beta}) \partial_{1\alpha} \rho u_\beta. \tag{3.25}$$

(Here we have not yet substituted the coefficients a, b, e, and h in the equilibrium distribution.) Now we can substitute $F_i^{(1)}$ into the first order term $\Pi^{(1)}_{\alpha\beta}$ of the momentum tensor [29]:

$$\begin{aligned} \epsilon \Pi^{(1)}_{\alpha\beta} &= \epsilon \sum_{i=1}^{8} m_i v_{i\alpha} v_{i\beta} F_i^{(1)} && (3.26) \\ &= \eta v^2 \xi [(12a - 4b) \delta_{\alpha\beta} \nabla \cdot \rho \mathbf{u} \\ &\quad -4b(\partial_\beta \rho u_\alpha + \partial_\alpha \rho u_\beta)]. && (3.27) \end{aligned}$$

(We have used $\epsilon \partial_{1\gamma} = \partial_\gamma$.) On the other hand, we can substitute $F_i^{(0)}$ into $S^{(0)}_{\alpha\beta\gamma}$, and find [29] that

$$\begin{aligned} S^{(0)}_{\alpha\beta\gamma} &= \sum_{i=1}^{8} m_i v_{i\alpha} v_{i\beta} v_{i\gamma} F_i^{(0)} && (3.28) \\ &= \frac{v^2}{3} \rho (u_\gamma \delta_{\alpha\beta} + u_\beta \delta_{\alpha\gamma} + u_\alpha \delta_{\beta\gamma}). && (3.29) \end{aligned}$$

Equations (3.18), (3.27) and (3.29) can finally be substituted into Eq. (3.22) and, after some algebra, we find [29]

$$\begin{aligned}
&\partial_t \rho u_\alpha + \rho u_\beta \partial_\beta u_\alpha + u_\alpha \nabla \cdot \rho \mathbf{u} = \\
&-\partial_\alpha p + \eta v^2 \left(\frac{\xi}{3} - \frac{1}{6} \right) \nabla^2 \rho u_\alpha + \\
&\eta v^2 \left[\xi (\frac{2}{3} - 12a) - (\frac{1}{3} - 6a) \right] \partial_\alpha \nabla \cdot \rho \mathbf{u}.
\end{aligned} \tag{3.30}$$

In the case of an incompressible fluid, $\nabla \cdot \rho \mathbf{u} = 0$, and we get the usual Navier-Stokes equation

$$\partial_t \mathbf{u} + (\mathbf{u} \cdot \nabla)\mathbf{u} = -\frac{1}{\rho} \nabla p + \nu \nabla^2 \mathbf{u}, \tag{3.31}$$

where

$$\nu = \eta v^2 \frac{2\xi - 1}{6} \tag{3.32}$$

is the kinematic viscosity of the lattice-Boltzmann fluid. (Here the term $\nu_{\text{latt}} = -\eta v^2/6$ is caused by the lattice dicreteness.) It is evident from Eq. (3.32) that the kinematic viscosity ν is independent of fluid density. Also, one can get an arbitrarily small viscosity for $\xi \to \frac{1}{2}$. However, viscosity must not be too small as the dissipation length scale should always be much bigger than the lattice spacing λ [29]. The lattice-Boltzmann algorithm may furthermore become unstable for very small values of ξ.

3.3 Other lattice-Boltzmann models

In the literature different formulations of the lattice-BGK model can be found. The differences lie *e.g.* in the use of rest particles, and in the connectivity of the lattice being used.

In two dimensions the most common model is the D2Q9 model, which is the D2Q8 model with a rest particle included. (We have used this model in our 2D lattice-Boltzmann simulations.) As the lattice-Boltzmann method was originally developed from the lattice-gas model, the first lattice used in 3D simulations was the D3Q19 lattice [7], which is a 3D projection of the 4D face-centered hyper-cubic (fchc) lattice used in 3D lattice-gas simulations. In this model each lattice point is connected with its six nearest and twelve next-nearest neighbours (see Fig. 4.4). Later it was realized that the relative freedom in choosing the lattice-Boltzmann equilibrium distribution also gave

Model	0	I	II	III
D2Q9	4/9	1/9	1/36	0
D3Q15	2/9	1/9	0	1/72
D3Q19	1/3	1/18	1/36	0

Table 3.1: The coefficients m_i in the equilibrium distribution $f_i^{(0)}$ for the different lattice-BGK models [13, 55]. 0 indicates a rest particle, I is for links pointing to the nearest neighbours, II is for the links pointing to the next-nearest neighbours, and III is for the next-next-nearest neighbours.

some freedom in choosing the structure of the simulation lattice. As a result, the D3Q15 model was developed [13]. In this model each lattice point is connected with its six nearest and eight next next-nearest neighbours (see Fig. 4.4). In both these 3D models rest particles are included.

The D3Q14 and D3Q18 models are obtained from the D3Q15 and D3Q19 models, respectively, by excluding the rest particles. However, the presence of rest particles is often desirable for improving the accuracy of the model (rest particles remove the unphysical velocity dependence of pressure) [57]. Also, for a small relaxation time ξ, the rest particles may be needed to stabilize the system [56]. Therefore, the D3Q15 and D3Q19 models are most often used in practical simulations.

The computational intensity and memory requirements of the lattice-Boltzmann model scale linearly with the number of fluid particles. The D3Q14 and D3Q15 models are thus somewhat more efficient than the D3Q18 and D3Q19 models. However, in the D3Q14 and D3Q15 models there can appear checkerboard behaviour in the fluid momentum, *i.e.*,the momentum may form unphysical regular patterns. This will be demonstrated in Chapter 4.

There are several possible realizations for the equilibrium distributions of these models (see Refs. [13, 55, 58, 59]). One choice is [13]

$$f_i^{(0)} = m_i \rho \left(1 + \frac{1}{c_s^2}(\mathbf{v}_i \cdot \mathbf{u}) + \frac{1}{2c_s^4}(\mathbf{v}_i \cdot \mathbf{u})^2 - \frac{1}{2c_s^2}u^2 \right), \qquad (3.33)$$

where $c_s = 1/\sqrt{3}$ is the speed of sound. The weight factors m_i for the D2Q9, D3Q15 and D3Q19 models are shown in Table 3.1 [13, 55]. In these models,

the kinematic viscosity is $\nu = (2\xi - 1)/6$ [13], and the fluid pressure is

$$p(\mathbf{r}, t) = c_s^2(\rho(\mathbf{r}, t) - \bar{\rho}) \equiv c_s^2 \Delta\rho. \tag{3.34}$$

Here $\bar{\rho}$ is the mean density of the fluid.

The lattice-Boltzmann method is very flexible. It can be modified to many different problems, such as multiphase flows [14, 27, 60, 61, 62, 63], suspension flows [15, 58, 64, 65, 66, 67], thermodynamics [68, 69, 70], growth processes [71], turbulence [72, 73], magnetohydrodynamics [74], reactive systems [75], non-Newtonian flows [76], and flows in complex geometries. There are also models for non-uniform lattices [77, 78, 79].

Chapter 4

Some practical problems in the lattice-gas and lattice-Boltzmann models

In this chapter we discuss several more or less practical problems related to the lattice-gas and lattice-Boltzmann models. In the first section general problems related to these models are discussed. In the following two sections these models are discussed separately. In the last section the parallelization of the lattice-Boltzmann model is discussed.

4.1 General remarks

The numerical quality of lattice-gas and lattice-Boltzmann simulations are determined mainly by the following error sources [V, 6, 59, 80, 81, 82]:

1. Finite-size effects. They are caused by insufficient number of lattice points in the smallest pores and obstacles of the flow system compared to the mean free path of the fluid particles.

2. Compressibility errors. They are caused by variations in density that violate the assumption of incompressible flow. These variations are caused by the fact that, in these methods, small fluctuations in the density are associated with variations in pressure.

3. Boundary effects. In principle, these methods are second-order convergent in space. However, close to the boundaries this convergence may be violated.

Moreover, in lattice gases the statistical fluctuations are an important source of error. In practice one cannot easily separate the errors caused by these various effects, but the total error can often be estimated by simulating the problem for several system sizes.

4.1.1 Implementation of solid boundaries

In lattice-gas and lattice-Boltzmann simulations the no-slip boundary condition is usually realized using the bounce-back condition [83, 84, 85]. In this approach the momenta of particles meeting the wall points are simply reversed. Bounce back can be applied either at wall points or in the middle of the streaming phase halfway between the fluid and solid points. For stationary flows these approaches are equivalent.

The bounce-back boundary generates errors which may violate the second-order spatial convergence of these methods. In lattice gases, *e.g.*, it creates a Knudsen boundary layer close to the walls [31, 83, 84].

The validity of the bounce-back condition has been widely discussed in particular in the case of the lattice-Boltzmann method [V, 80, 82, 85]. In simple shear flows, this condition determines the location of the wall to be exactly halfway between the last fluid point and first wall point. In more complicated cases the no-slip boundary usually is *somewhere* between the last fluid point and the first wall point, the exact place depending on the relaxation parameter and the geometry of the system [V, 86]. More sophisticated boundaries, which model a no-slip boundary exactly at the wall node (the so-called second-order boundaries), have been proposed by several authors, but unfortunately most of them are restricted to regular geometries (like flat walls and octagonal objects) [59, 80, 82]. For practical simulations the bounce-back boundary is very attractive, because it is a simple and computationally efficient method for imposing no-slip walls in irregular geometries.

Finally notice that, in Ref. [87], a model for arbitrary boundaries (*i.e.* cutting through the lattice links) is presented.

4.1.2 Pressure boundaries, velocity boundaries, and body force

Successful numerical simulation of practical fluid-flow problems requires that the velocity and pressure boundary conditions of the system have been imposed in a consistent way. However, general velocity and pressure boundaries are still under development for both the lattice-gas and the lattice-Boltzmann method. So far most of the practical simulations have used a body force [14, 31, 88] instead of pressure or velocity boundaries.

When a body force is used, a pressure gradient acting on the fluid is replaced by a uniform external force. (Usually periodic boundaries are imposed at least in the direction of the flow.) The use of a body force is based on the assumption that the effect of an external pressure gradient is approximately constant all over the system, and that it can be replaced by a constant force that adds at every time step a fixed amount of momentum to fluid particles.

In the lattice-gas model a uniform body force is obtained by changing at each time step at randomly chosen lattice points the momenta of particles in a preferred direction. In the lattice-Boltzmann method body force is simulated by adding at each time step a fixed amount of momentum to all fluid particles within the void volume. This addition can be done in several ways. We have added the momentum to links with a nonzero projection in the direction of the force, taking into account the weights m_i of the links.

In a simple tube flow the body-force approach is exact. In more complicated geometries this approach is supposed to work best with small Reynolds numbers, because then nonlinear effects on the flow are small.

4.1.3 Some effects of lattice discreteness

In Fig. 4.6 we show the surface of a sphere in one plane of a cubic lattice. It is evident that the surface is quite rough. In traditional CFD the computation grid can be made denser close to the surfaces, and the location of the grid points can be chosen freely. In the simplest lattice-gas and lattice-Boltzmann models this is not possible. Fluid, however, tends to "smooth" rough surfaces [V, 89]. In Ref. [2], *e.g.*, 2D fluid flow around a smooth cylinder and a pathologically rough cylinder was simulated with the lattice-gas method. The difference between the simulated drag forces was only 4%, although the variation in the radius of the rough obstacle was as much as 10%. Smoothing is also seen in the values of hydrodynamic radii a of vari-

a_0	1.5	2.5	4.5	8.5	16.5
a	1.36	2.43	4.49	8.53	16.54

Table 4.1: The actual radii a_0 and the averaged hydrodynamic radii a for randomly placed 2D cylinders.

a_0	1.5	2.5	4.5	8.5
a	1.54	2.61	4.53	8.47

Table 4.2: The actual radii a_0 and the averaged hydrodynamic radii a for randomly placed 3D spheres.

ous obstacles in lattice-Boltzmann simulations. (The hydrodynamic radius can often be derived by simulating fluid flow in an infinite array of obstacles [15].) For $\xi = 1.0$, *e.g.*, one finds $a = 5.56$, 11.56 for 2D cylinders with actual radii of $a_0 = 5.5$, 11.5, respectively. (The centre of the cylinder has been placed on a lattice point.) So, the apparent roughness of the surface does not necessarily have a big effect on the accuracy of the simulations. (The things are, however, made a little more complicated by the fact that a may depend quite strongly on ξ as we will see below.)

If the obstacles move, as is the case in suspension simulations, their shapes vary in time due to the lattice discreteness. In such cases the discreteness of the system can be taken into account by averaging the hydrodynamic radius over a large sample of randomly placed obstacles. We show in Table 4.1 the averaged hydrodynamic radii for 2D cylinders in the case $\xi = 1.0$ [90]. The corresponding values for 3D spheres are shown in Table 4.2 [15].

4.1.4 Finite-size effects

The accuracy of lattice-gas and lattice-Boltzmann simulations depend on the ratios of the mean free path λ_{mfp} of the fluid particles to the sizes of the obstacles and pores [6, 14, 88, 91, 92, 93]. The simulated flow field does not display true hydrodynamic behaviour unless these ratios are small. This kind of *Knudsen-flow* behaviour is found also in real fluids [17]. These

effects must always be considered when lattice-gas and lattice-Boltzmann simulations are performed. They determine the minimum size of the pores and the obstacles, and thus also the minimum size of the simulation lattice.

Finite-size effects restrict to some extent the use of the lattice-gas and lattice-Boltzmann methods. In porous media close to the percolation threshold, *e.g.*, many pores are very small, and very big lattices may be needed to perform realistic simulations. It is not clear, however, whether the finite-size effects are always dominated by the *minimum pore size*, or could sometimes the *average pore size* be more important. One has to also remember that in some applications, the qualitative structure of the flow field may be enough [II, III]. So, with each application, the importance of finite-size effects must be estimated separately.

4.1.5 Staggered invariants

In the lattice-gas and lattice-Boltzmann models, the basic ingredients of the dynamics are the local conservation of mass and momentum. Of course, it is not desirable to have any other unphysical conserved quantities, spurious invariants, in the dynamics. As we have discussed before, one problem of the HPP model was that the momentum along each vertical and horizontal line was also conserved. One could get rid of these quantities in the FHP model. However, in all lattice-gas and lattice-Boltzmann models the discrete nature of the system creates another class of spurious invariants, called *staggered invariants* [15, 29, 30]. They have obtained this name because they depend on the parity of space and time. Staggered invariants may play an important role in the behaviour of the lattice-gas and lattice-Boltzmann models [29, 30]. The influence of staggered invariants, however, can be minimized by properly choosing the initial condition of the fluid particles [29, 30]. Spatial or temporal averaging can also be used to eliminate them [15].

4.1.6 Saturation time in steady-state simulations

In permeability simulations, *e.g.*, a simple dimensional analysis shows that, for a constant body force, the saturation time t_{sat} needed to reach the steady state is of the form

$$t_{\text{sat}} \propto R_{\text{pore}}^2/\nu, \tag{4.1}$$

where R_{pore} is the characteristic length of the void pores in the system and ν is the kinematic viscosity of the fluid. For systems with high porosity ϕ, the saturation times can therefore be very long. In some cases, tens of thousands

of time steps may be needed. It is thus evident that a constant body force can be computationally inefficient, especially when one is only interested in the steady-state solution. (In standard computational fluid dynamics, this problem can be overcome by solving the time-independent flow rather than the complete Navier-Stokes equation.)

In time-dependent flows, accurate initial conditions are obligatory [59], whereas in time-independent flows, properly chosen initial conditions may be used to speed-up saturation. Such conditions cannot be easily found directly. However, if the essential dimensionless numbers, like the Reynolds number, are kept constant, the simulations may first be carried out either on a smaller lattice or for a clearly higher viscosity. In both cases the simulation time will be smaller than in the original system. Due to discretization errors and finite-size effects, the obtained velocity and pressure fields may be quite inaccurate, but they can be used as good initial guesses for the final simulation.

The saturation time can also be reduced by using the Iterative Momentum Relaxation (IMR) method, where the applied body force is adjusted during the iteration in a definite relation to the change in the fluid momentum during iteration steps. This method is described in detail in Ref. [V].

4.1.7 The numerical efficiency of the lattice-gas and lattice-Boltzmann models

In the standard lattice-gas model 24 bits are needed to describe a particle configuration in 3D, whereas in the lattice-Boltzmann model 15 – 19 real numbers must be used. Also, the lattice-Boltzmann collision operator requires several floating point operations whereas the lattice-gas collisions can be realized with simple look-up tables. Thus, one could expect that the lattice-Boltzmann method is computationally much more intensive and has significantly higher memory requirements than the lattice-gas method. However, in the lattice-gas simulations the spatial and temporal averaging that are needed for extracting smooth hydrodynamic fields severely decreases the performance of the method. Also, due to the relatively high fluid viscosity, big lattices are needed for high Reynolds-number simulations. So, for low Reynolds numbers and for such applications where only the average fluid velocity is needed (this is *e.g.* the case when the permeability of a porous medium is being determined), the lattice-gas method may be more efficient [14]. However, for high Reynolds-number flows, and when a detailed knowledge of the hydrodynamic fields is required, the lattice-Boltzmann method is likely to perform better [94].

The performance of lattice-gas and lattice-Boltzmann methods against more conventional methods strongly depends on the application. Without a local grid refinement, these methods are computationally rather inefficient in many practical engineering problems if the geometry of the system is relatively simple. However, this inefficiency may often be more than compensated by the total time spent on solving a problem, as grid generation is often the most time-consuming part with traditional methods. Parallel computing can also be used to surpass this problem.

Generally speaking, the more complicated the fluid-flow problem is, the more efficient the lattice-gas and lattice-Boltzmann methods are expected to be. The performance of these models should thus be relatively high for such applications as multiphase flows, suspension flows, and flows in complex geometries. However, specific head-to-head comparisons that would verify this view are very rare. In this respect Ref. [95] is perhaps the most thorough study to date. In this reference a detailed comparison between the finite-element and the lattice-Boltzmann methods was presented for a 3D fluid flow in a static mixer used in industrial processes. The geometry of this mixer, although not yet very complicated, is already quite a challenge for traditional simulational methods. The lattice-Boltzmann method was found to be less memory consuming for this particular application. The computational times were similar in both cases, but the IMR-method (described in the previous section) would have improved the performance of the lattice-Boltzmann method. It was also found that the lattice-Boltzmann method gave reasonable pressure and velocity fields with both the lattice resolutions used, while the pressure fields given by the finite-element method were quite sensitive to the computational grid used. We can thus conclude that, for systems with very complicated boundaries, the lattice-gas and lattice-Boltzmann models are likely to perform better than most traditional methods.

4.2 The lattice-gas model

4.2.1 Reynolds number

The dimensionless form of the Navier-Stokes equation Eq. (1.3) is [1]

$$\partial_{t^*}\mathbf{u}^* + (\mathbf{u}^* \cdot \nabla^*)\mathbf{u}^* = -\nabla^* p^* + \frac{1}{\mathrm{Re}}\nabla^{*2}\mathbf{u}^*. \tag{4.2}$$

(The external force has been omitted.) Here Re is the Reynolds number which is defined as

$$\mathrm{Re} = \frac{UL}{\nu}, \tag{4.3}$$

where U and L are the typical velocity and length scales of the system, respectively, and ν is the kinematic viscosity of the fluid. Two systems are dynamically similar if their Reynolds numbers (and system geometries) are essentially identical. The similarity of Reynolds numbers is very important when simulation results or model experiments are applied to real systems.

In the FHP-models the Reynolds number is [4, 29]

$$\mathrm{Re} = \frac{LUg(\rho)}{\nu(\rho)}. \tag{4.4}$$

The $g(\rho)$-term appears here due to rescaling of time, which leads to rescaling of viscosity $\nu(\rho) \to \nu(\rho)/g(\rho)$.

4.2.2 Finite-size effects

Several authors have studied the problem of finding a reasonable size for pores and obstacles [6, 88, 91, 92, 93] in lattice-gas simulations. It is suggested in Ref. [91] that, in lattice-gas simulations, permeability obeys the scaling law

$$k = k_\infty(1 + \alpha/R), \tag{4.5}$$

where R is the characteristic size of the system in lattice units, α is a constant that depends on the details of the simulation model used, and k_∞ is the asymptotic permeability of the system (*i.e.* the permeability that would be obtained for an infinite lattice).

We studied for $\rho = 3.5$ the size dependence of permeability in a system of randomly placed rectangles with a side length of $L/10$, L being the linear lattice size. (see Fig. 5.5). The asymptotic values k_∞ were derived by fitting Eq. (4.5) to the simulated points.

It is evident from Fig. 4.1 that the predictions given by Eq. (4.5) agree well with the simulated results. Also, the 40×40 rectangles that were used in the permeability simulations give an accuracy better than 5% when porosity ϕ is larger than 0.5. (Notice that for high porosities the obstacle size, and for low porosities the pore size, dominate the finite-size effects. For this reason the error increases with decreasing porosity.)

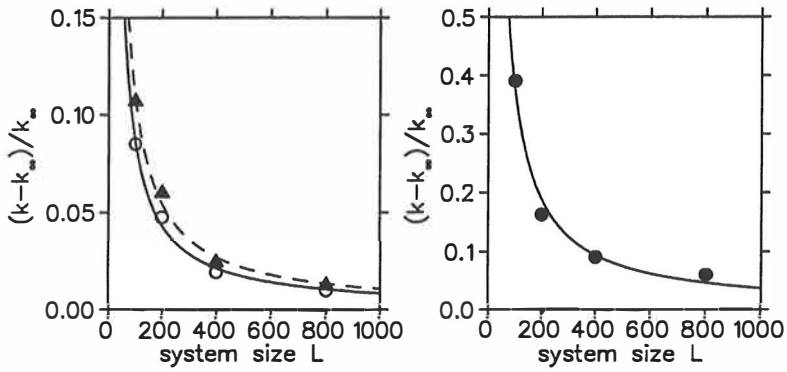

Figure 4.1: The relative error in permeability as a function of system size L. The linear size of the rectangle is $L/10$. Left: Open circles and the solid line show the result for a system with $\phi = 0.76$. Solid triangles and the dashed line show the result for a system with $\phi = 0.59$. Right: The results for a system with $\phi = 0.49$.

4.2.3 Statistical noise

The boolean nature of the lattice gas makes its dynamics noisy. Noise can be damped with a spatial or temporal averaging of particle velocities, but the smaller is the fluid velocity, the longer one has to average to get the given accuracy. The number of averaging time steps may thus give a practical lower limit for the local fluid velocity.

We derive an equation for the absolute error $\Delta u_{\mathrm{ave}}(T)$ due to the noise in fluid velocity averaged over T times at one lattice point. We take pure fluid with density $\rho = 3.5$ and velocity $u = 0.0$. In such a system all the 128 possible particle configurations are equally probable, and the standard deviation of either component of the fluid-momentum vector is $\delta p = 0.866$ at each lattice point. Therefore, the absolute error in both velocity components is given by

$$\Delta u_{\mathrm{ave}}(T) \approx \frac{\delta p}{\rho\sqrt{T}}. \tag{4.6}$$

For nonzero fluid velocities all particle configurations are not equally probable. However, the differences in these probabilities are small, and Eq. (4.6) can also then be used to determine the statistical error in velocity.

We checked the validity of Eq. (4.6) in the case of $u = 0.07$. The results are shown in Fig. 4.2. The thick line shows the prediction given by Eq. (4.6), and the thin line shows the simulated error. Clearly Eq. (4.6) compares

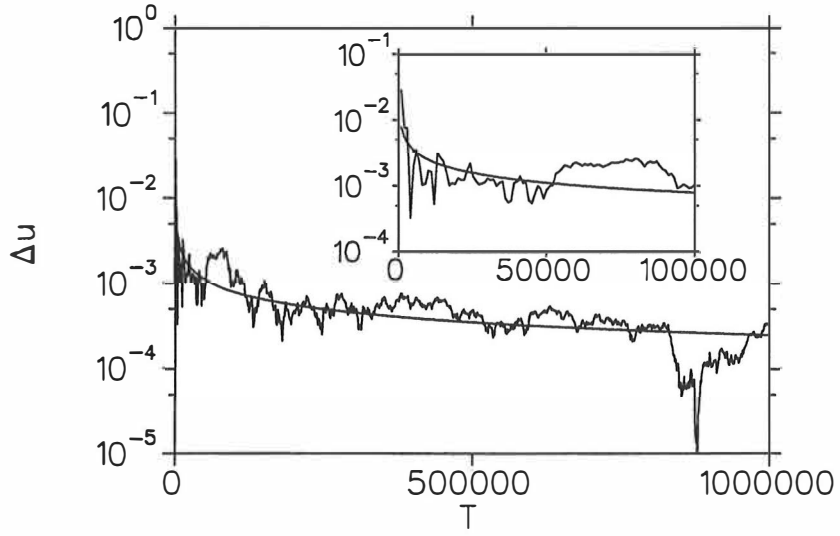

Figure 4.2: The absolute error Δu_{ave} in fluid velocity as a function of averaging time T. The thick line is the prediction given by expression Eq. (4.6). The thin line shows the simulation results. (The inset figure shows the error during the first 100000 time steps.)

reasonably well with the simulated results.

Notice that in many cases (*e.g.*, when the permeability of a porous sample is determined) only the total fluid momentum is needed. In such cases the averaging time can be quite small. Good accuracy is usually obtained within a few hundred or thousand time steps.

4.2.4 Viscosity

The analytic derivation of the lattice-gas viscosity requires several simplifications, and Eqs. (2.48) and (2.51) are thus only approximations. For this reason the viscosity is usually determined by direct simulations. There are several ways to do this: a simple tube flow [88], relaxation of a periodic perturbation [96], and a channel flow in which there are two components flowing in opposite directions [31, 97]. The problem with tube flow is that the boundary layer generated close to the walls will decrease the accuracy of the simulation [31]. For this reason the two latter methods are recommended. The simulations presented in Refs. [31, 96] show that the expression Eq. (2.51) gives the viscosity with quite good acccuracy. Deviations from

ν	$\frac{1}{1536}$	$\frac{1}{96}$	$\frac{1}{24}$	$\frac{1}{12}$	$\frac{1}{6}$	$\frac{1}{3}$	$\frac{2}{3}$	$\frac{8}{3}$
a	5.12	4.79	4.67	4.60	4.53	4.42	4.27	3.70

Table 4.3: Dependence of the hydraulic radius a on the kinematic viscosity ν. The actual radius is $a_0 = 4.5$.

the theoretical values are 5 – 15% in a density range of $1.4 \leq \rho \leq 3.5$ for moderate lattice sizes.

Notice also that the viscosity of 2D lattice gases diverges logarithmically with increasing system size [31]. (In the lattice-Boltzmann models this behaviour is not found.) In the FHP-III model this effect vanishes for $\rho = 3.5$.

4.3 The lattice-Boltzmann model

4.3.1 Shift of the boundary. Finite-size effects

As discussed above, the exact location of the solid-fluid boundary is dependent on the value of the relaxation parameter ξ and the geometry of the system. Factor ξ also gives the mean free path of the lattice-Boltzmann fluid, thereby determining the minimum length scale (in lattice units) for true hydrodynamic behaviour of the fluid. It is not easy to separate the errors caused by these effects, so we will give some examples of how they are manifested in practice.

In Ref. [V] we studied the location of the boundary in the case of simple Poiseulle flow in a tilted tube. We found that the lattice-Boltzmann method is second-order convergent for both flat and regular saw-tooth boundaries, provided that the no-silp wall is taken to be exactly halfway between the solid walls and the adjacent boundary node. The exact location of this wall depends on the relaxation parameter ξ.

In Table 4.2 the dependence of the hydrodynamic radius a on the actual radius a_0 was shown for $\xi = 1.0$. Surprisingly small spheres, even those of $a_0 = 1.5$, were found to have a reasonable hydrodynamic radius. This radius depends, however, quite strongly on the value of the relaxation parameter. For an actual radius of $a_0 = 4.5$, *e.g.*, the hydrodynamic radii corresponding to different values of $\nu = (2\xi - 1)/6$ are [15] given in Table 4.3. It is evident, that for the highest and lowest viscosities deviation of the hydrodynamic radius from the actual radius is quite large. (For the highest viscosity the

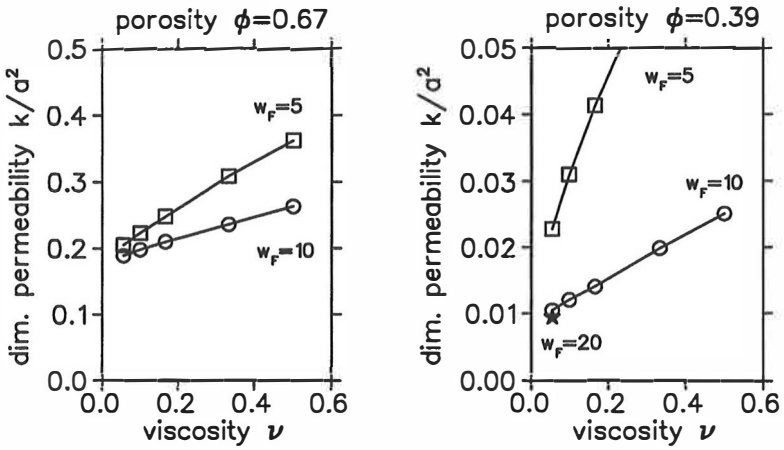

Figure 4.3: Simulated dimensionless permeability k/a^2 of a 3D random fibre web as a function of viscosity ν for two different porosities. Here $a = w_F/2$, and (in lattice units) the fibre widths w_F were w_F=5 (squares), 10 (circles) and 20 (star).

mean free path is too long in comparison with to the actual radius of the obstacle, and for the smallest viscosity the dissipation length is too short in comparison with the lattice spacing.)

In Ref. [14] the finite-size effects related to permeability simulations of fluid flow in a tomographic model of sandstone were studied. The permeability of the porous sample was there shown to depend approximately linearly on the fluid viscosity. We have performed corresponding simulations for fluid flow through 3D random fibre webs. (For details of these simulations see the next Chapter 5.) In Fig. 4.3 we show the simulated permeability as a function of fluid viscosity ν for two webs with different porosities. For $\phi = 0.67$, the result is seen to be almost independent of the grid resolution for the smallest value of viscosity. For $\phi = 0.39$ finite-size effects become more pronounced. For the smallest viscosity, a fibre thickness of $w_F = 10$ seems to give the accuracy of about 15%. (The error estimate was done by extrapolating the permeability curves to $\nu = 0$.)

We have also studied in the 2D case the hydrodynamic forces acting on a cylinder close to a moving wall. (The wall velocity v_w was 0.05, and the relaxation parameter was $\xi = 1.0$.) The gap between the wall and the cylinder (with an actual radius of $a_0 = 11.5$) was in these simulations even as small as one lattice spacing. The results were compared with those given

by a traditional finite-difference code.

The results were surprisingly good. The difference in the drag forces as determined by the two methods remained below 1%, even when the gap between the cylinder and the wall was only one lattice spacing. The maximum difference in the lift forces, namely 6%, was obtained for a gap of 4 lattice spacings. (For details of this comparison see Ref. [98].) Corresponding simulations were also performed for $a_0 = 5.5$. In this case the differences in the drag and lift forces for a gap of 4 lattice spacings were about 4% and 14%, respectively.

4.3.2 Body force

In order to check the validity of the body-force approach, we simulated 2D fluid flow through a vertically infinite array of cylinders with both the body force and pressure boundaries [V]. Pressure boundaries were implemented by the method presented in Ref. [81]. The particle Reynolds number was Re= 0.4 in these simulations. The differences between the results were small: close to the cylinder, the average errors in the velocity and pressure fields remained well below 0.5%, whereas the maximum errors were smaller than 1.0%.

Thus, for small Reynolds numbers and simple boundary conditions, the body-force approach seems quite an accurate substitute to pressure boundaries. However, for high Reynolds-number flows, where nonlinear effects are dominant, and for more complicated boundary conditions, explicit velocity and pressure boundaries may be needed.

4.3.3 Checkerboard effect in the D3Q14 and D3Q15 models

In the D3Q14 and D3Q15 models there can be checkerboarding in fluid momentum, *i.e.*, fluid momentum may form unphysical regular patterns as we have demonstrated in Ref. [V].

Let us mark the lattice points (i, j, k) by black colour if $i+j+k$ is odd, and by white colour otherwise. A checkerboard pattern shown in Fig. 4.4 for the D3Q19 and D3Q15 models is thus formed. To each lattice-Boltzmann fluid particle, we also assign the colour of the lattice point at which they are in the beginning of the simulation. If there are no obstacles in the system, it is easy to see that, in the D3Q14 model, the black and white particle populations are completely independent of each other: the colour of the lattice point at which a given fluid particle resides changes at every time step (see Fig. 4.4). As a

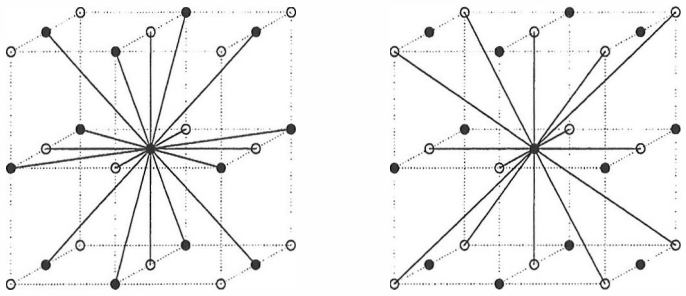

(a) The D3Q19 model.

(b) The D3Q15 model.

Figure 4.4: Lattice structures of the D3Q19 and D3Q15 lattice-BGK models. The checkerboard colouring is also shown in the figures.

consequence of this checkerboard effect, the total mass and momentum of the black- and white-particle populations are spurious invariants, *i.e.* unphysical conserved quantities in the D3Q14 model. Similar spurious invariants are also found in the HPP lattice-gas model [3]. These invariants can create unphysical hydrodynamic modes in the simulated system, and for this reason they should usually be eliminated from the model [6]. Notice that, in the D3Q18 model, the black and white populations mix immediately with each other. Consequently, there is no checkerboard effect in this model.

In the D3Q15 model the black and white populations are not entirely independent as they are coupled through the rest particles. However, checkerboard effect may also here lead to unphysical behaviour. If the lattice is initialized with equilibrium distributions, such that , *e.g.*, the velocity is set to $\mathbf{u}_b$ at the black lattice points and to $\mathbf{u}_w$ at the white lattice points, while $|\mathbf{u}_b|$ is equal to $|\mathbf{u}_w|$, it is easy to see that the total momenta of the black and white populations will be conserved quantities.

We studied the checkerboard effect in the D3Q15 model by following the relaxation of a perturbed velocity field for a constant initial density and with periodic boundaries imposed in all directions. We found that, on a $10 \times 10 \times 10$ lattice, fluid remained partialy unmixed in the steady state. This behaviour was not found in the D3Q19 model.

Similar simulations were also performed on a $9 \times 9 \times 9$ lattice. In this case the two populations had additional mixing at the boundaries of the lattice, as the colouring rule was there uncontinuous due to the length of

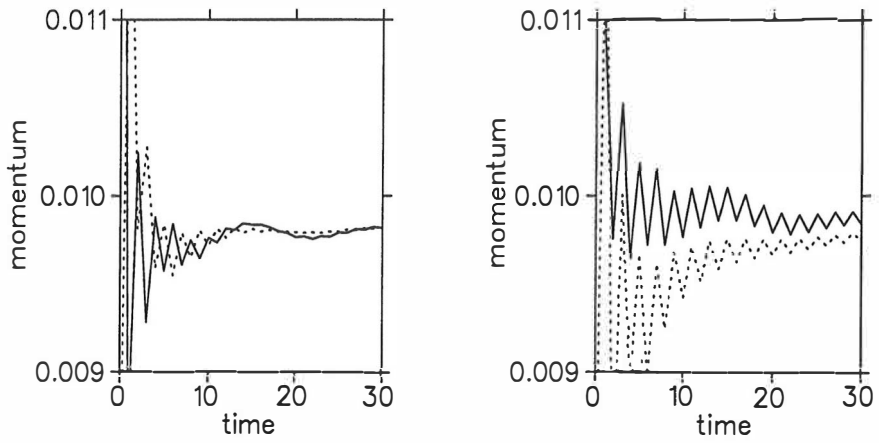

(a) D3Q19 model

(b) D3Q15 model

Figure 4.5: Relaxation of the x component of the momentum at two next-nearest neighbour sites in the xy plane of a lattice of dimension $9 \times 9 \times 9$. The initial perturbed velocity field is the same in both models.

the lattice being an odd number. As a result, the steady-state momentum field was uniform for both models. However, the weak coupling between the black and white populations in the D3Q15 model was still apparent in the time evolution of the relaxation process. This can be seen in Fig. 4.5, where relaxation of the momenta at two next-nearest neighbour sites is shown in one direction. In the D3Q15 model the relaxation process is seen to be significantly slower, and there are in this case long-lasting oscillations in the local values of the momentum.

We studied the checkerboard effect also in the presence of solid walls. The first test case was fluid flow in a rectangular duct. In this case no checkerboarding was seen. The second test case was fluid flow in a regular array of spheres. In this case, the checkerboard effect did not lead to momentum oscillations, but the velocity and pressure fields included unphysical regular patterns. In Fig. 4.6a we show the relative difference ϵ_v between the velocity fields obtained by the D3Q19 and D3Q15 models. Fluid is flowing from left to right and periodic boundaries are used in both directions. The gray-scale colours change from white to black in the scale $-3.0\% \leq \epsilon_v \leq 3.0\%$. In Fig. 4.6b we show the velocity profile at the inlet of the system for both

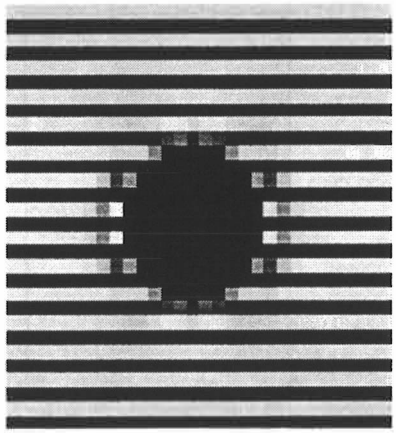

(a) The relative difference ϵ_v of the velocity fields determined by the D3Q19 and D3Q15 models.

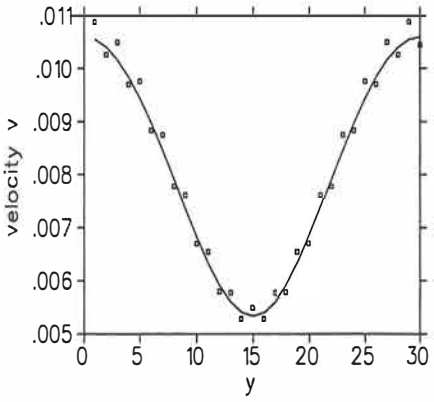

(b) The velocity profiles at the inlet. Solid line: the D3Q19 model. Open squares: the D3Q15 model.

Figure 4.6: Comparison of the D3Q15 and D3Q19 simulations of fluid flow in a regular array of spheres.

models. The solid line and open squares show the results for the D3Q19 and D3Q15 models, respectively. Patterns are clearly seen in both these figures. Despite these unphysical effects, the averaged values in the D3Q15 model, such as the average momentum of the fluid, were very close to the corresponding values of the D3Q19 model.

We can conclude that, in the D3Q15 model, there is a checkerboard effect which may appear in the hydrodynamic fields. In some cases boundary effects can suppress this unphysical feature. Furthermore, it does not have a significant effect on global values such as the average fluid momentum. Therefore, in spite of its shortcomings, the D3Q15 model appears a viable alternative for steady-state hydrodynamics.

As Fig. 4.5 demonstrates, in dynamical systems (*e.g.* in fluid-particle suspensions or in turbulence simulations) the checkerboard effect may slow down the relaxation of momentum and can, in principle, induce unphysical effects on the dynamics of the system. Notice, however, that solid boundaries increase mixing also in the D3Q15 model when bounce back on the links is used at the boundaries.

4.4 Parallelization of the lattice-Boltzmann model

Realistic lattice-gas and lattice-Boltzmann simulations often require large computational resources and, therefore, are executed on parallel systems. Fortunately, the inherent spatial locality of the updating rules of these methods makes them ideal for parallel processing.

In this section we briefly discuss the parallelization of the lattice-Boltzmann method and present the results of a few performance studies of our 3D lattice-Boltzmann code. This code has been quite heavily optimized by reducing as far as possible the computations related to the application of the collision and propagation rules. Also, the order of loops have been designed such as to minimize the number of cache misses. With the optimized code, an increase in speed by a factor 5 has been achieved as compared to a naive implementation of the lattice-BGK evolution rule. The code has been implemented in C using the MPI message-passing library [99].

4.4.1 Data decompositions

Basically parallelization of the grid-based algorithms like those of the finite-difference, finite-element and lattice-Boltzmann models, is done by means of the data decomposition strategy in which the computational grid is decomposed into sub-domains [100]. Each processor performs computations in a certain sub-domain, and exchanges information with other nodes in order to resolve dependencies. The two factors controlling the efficiency of parallelization are the ratio between the communication and computation times, and the balance of workload among the processors. All previously reported parallelizations of the lattice-Boltzmann method are based on one-, two- or three-dimensional decompositions of the computational grid in equal sub-volumes, and load balancing is completely ignored for simplicity [82, 101, 102]. These decompositions give high efficiencies when workload is distributed homogeneously. (By a homogeneous workload distribution we mean that obstacles in the fluid are uniformly distributed over the lattice, while in a heterogeneous workload distribution this is not the case.) However, in many fluid-dynamical problems, workload may be highly non-homogeneous and sometimes can even vary dynamically during the simulation. We have introduced a new parallelization approach for the lattice-Boltzmann method based on the Orthogonal Recursive Bisection method [IV]. With this approach high parallel efficiencies can be obtained also for heterogeneously distributed workloads, thus supporting efficient simulations

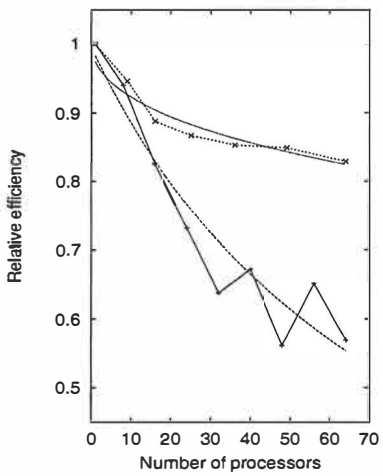

(a) The 100x100x60 lattice.

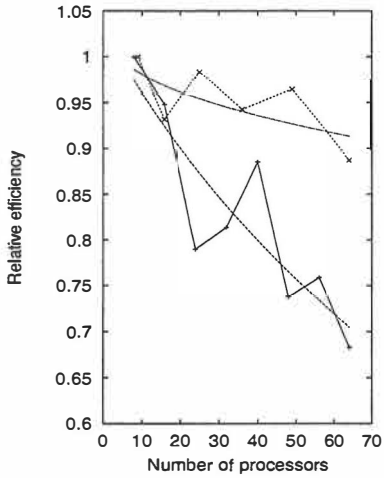

(b) The 200x200x110 lattice.

Figure 4.7: The relative efficiencies of the slice and box decompositions as a function of the number of processors. Solid lines (— + —) show the results for slice decomposition and dotted lines ($\cdots \times \cdots$) show the results for box decomposition. A least squares fit by the theoretical model [IV] is shown for both decomposition strategies.

of a variety of realistic systems.

4.4.2 Load balancing for homogeneous workload distributions

For problems with a homogeneous workload, parallelization can be done by means of a straightforward decomposition in equal sub-volumes of the computational grid. Decomposition may be done, *e.g.*, in one dimension ('slice decomposition') or in two dimensions ('box decomposition'). These methods depend only on the dimensions of the lattice and on the number of processors, while the geometry of the application itself is neglected. An important feature of the lattice-Boltzmann scheme in this context is the inherent spatial locality of the collision operator. Furthermore, interactions between processors are only required at the propagation step. The advantage of the slice and box decompositions is that the dependencies between the

processors are simple due to the regular connectivity of the lattice, and the fact that the partitions are of equal size.

We have studied the performance of our code in the case of fluid flow in 3D random fibre webs (see the next Chapter 5). The fibres have been placed randomly in the system, and the workload is thus approximately balanced allover the lattice. In Fig. 4.7 we show the measured relative efficiencies together with a fit by the corresponding analytic performance model to the simulated points (see Ref. [IV]). The computations were performed for two fibre webs of dimension $100 \times 100 \times 60$ and $200 \times 200 \times 110$ lattice points on a 64-node Cray T3E system.

The fluctuations of the data are caused by the effect of caching and load imbalance (when the number of lattice points is not evenly divisible by the number of processors). It is evident from these experiments that slice and box decompositions are both efficient and useful strategies for problems in which the workload is approximately homogeneous. Slice decomposition is relatively easy to implement, but its efficiency is seen to be satisfactory only when the number of processors is relatively small. For the box decomposition, the efficiency for a lattice of $100 \times 100 \times 60$ is still around 0.9 on 64 processors. Even for larger lattices efficiences close to one can thus be obtained with this decomposition strategy.

4.4.3 Load balancing for heterogeneous workload distributions

One of the main advantages of the lattice-Boltzmann method is its suitability for a large class of different geometries. However, for a heterogeneously distributed workload (*i.e.* for heterogeneous distribution of fluid points), slice and box decompositions can result in a considerable load imbalance. Consequently, the efficiency of the parallel program will decrease due to idle synchronization times. It is therefore important to study decompositions that can deal with heterogeneously distributed workloads. The need for such load-balancing approaches was already noticed in Ref. [59].

The first step in load balancing is to find a partitioning of the grid such that differences in the workload of the processors are minimized. There are several ways to accomplish this goal. We have chosen the ORB method [IV] for two reasons. First of all, from a practical point of view minimization of the computation time is more important than minimization of the communication time, and, in the lattice-Boltzmann method, the communication overhead is small for moderate lattice sizes [IV]. Secondly, the other

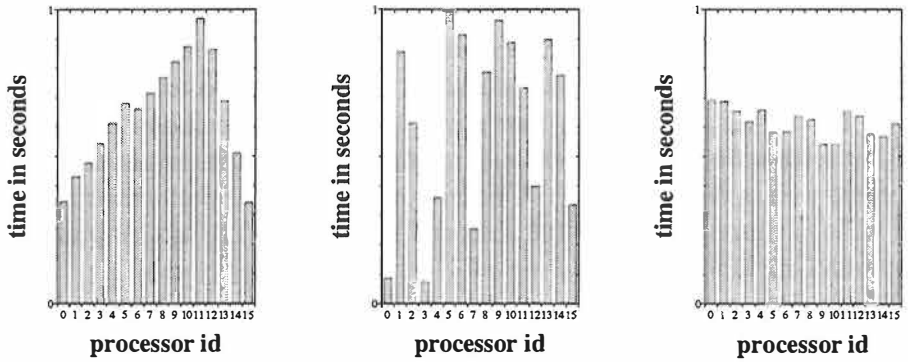

(a) Slice (b) Box (c) ORB

Figure 4.8: Execution profiles for the different decomposition strategies. The test problem is fluid flow in a tube of varying cross section.

strategies are usually quite expensive and should be used only when the communication time becomes significant.

We implemented the ORB strategy and performed timing measurements for a test problem of fluid flow in a tube of varying cross section [IV]. In Fig. 4.8 the load distributions for this test case are shown for different decomposition strategies. The workload is seen to be approximately balanced among the processors when the ORB method is used, while in the slice and box decompositions, big differences are seen in the computing times of the processors. It is thus evident that slice and box decompositions are inefficient for this application.

With $2 - 16$ processors the ORB method was found to be $20 - 60\%$ more efficient than the slice and box decompositions. Thus, for large-scale simulations (execution times of many hours), the benefit gained by load balancing will be significant. We would like to emphasize that the extra communication overhead due to the irregular communication pattern is here small. Extension of these ideas to dynamically varying workloads looks promising, especially because of this relatively small overhead.

Chapter 5

Simulations of single-fluid flow in porous media with lattice-gas and lattice-Boltzmann methods

In this chapter, we first discuss the problem of single-fluid flow in a porous medium in general, and briefly review the previous lattice-gas and lattice-Boltzmann studies on this topic. Then we discuss the basic physics of this problem. Here the concepts of tortuosity and effective porosity will receive special attention. We present our simulated results for tortuosity, effective porosity and permeability of a 2D random porous medium, and compare the simulated permeabilities with various theoretical predictions. Finally, we present our results for fluid flow in massive 3D random fibre webs, and show that these results compare very well with experimental data.

5.1 Fluid flow in porous medium

Transport and flow phenomena in porous media arise in many diverse fields of science and engineering, ranging from agricultural, biomedical, construction, ceramic, chemical and petroleum engineering to food and soil sciences and powder technology [23]. A classic example of the importance of improving our understanding of such processes is the high amount of unrecovered oil (50% or more) left in oil reservoirs by traditional recovery techniques [23].

Important problems are also the spread of hazardous wastes in soil, water removal in papermaking processes, and transport of water in biological materials (such as wood or hair) to name only few. In all these cases the porous structure of the medium is very complex and the relevant flow phenomena are difficult to study even in the case of single-phase flow in a static porous structure.

Studies of flow through porous medium have mainly been concerned with the derivation of macroscopic laws for the fluid flow. The basic question has been whether there is a general equation for the volumetric flow as a function of a pressure gradient acting on the fluid. Experiments have shown that, in the case of creeping flow of a single viscous fluid, the phenomenological law first discovered by Darcy [16, 17],

$$\mathbf{q} = -\frac{k}{\mu}\nabla p, \tag{5.1}$$

holds very well for a wide variety of natural porous media ranging from loose sand to tight granite rocks [17, 22, 23]. Here $\mathbf{q}$ is the flux of the fluid through the porous medium, μ is the dynamic viscosity of the fluid, and p is the fluid pressure. The coefficient k, permeability, is a measure of the fluid conductivity through the substance. (When fluid velocity is high, the functional relation between $\mathbf{q}$ and ∇p becomes nonlinear and Eq. (5.1) is not valid any more [23]. However, in most practical problems the fluid velocity is in the creeping flow regime.) Despite the great effort put on the studies of fluid flow in porous medium, many basic questions concerning permeability remain unanswered. Various correlations between the permeability and parameters describing the geometrical properties of the medium have been suggested, but a general equation for the permeability is still lacking.

Experimental methods have extensively been used to measure permeability and its dependence on material parameters. The methods used vary from rather straightforward measurements [18, 19, 20] to more sophisticated approaches, which utilize, *e.g.*, mercury porosimetry, electrical conductivity, nuclear magnetic resonance or acoustic properties of the medium [21]. A problem with experiments is that it is often difficult to accurately determine the relevant material characteristics affecting the permeability.

Theoretical methods typically rely on analytical models based on simplified pore geometries, allowing the solution of the microscopic flow patterns [22], or on more advanced methods that statistically take into account the structural complexity of the medium [22, 23]. A problem with theoretical

work is that usually major simplifications in the pore structure or flow dynamics are necessary to make the model mathematically reasonable. This often decreases the ability of the model to describe the real system.

Experimental and analytic work supplement each other. Due to the simplifications made, theoretical expressions usually include some parameters that can then be determined by experiments. Analytic work helps us to find general features of the given phenomenon and systematize the problem.

A third approach is numerical simulation. It interpolates between theory and experiments. Realistic 3D flow simulations in complex geometries are very demanding in terms of computing power. Until recently this approach has thus been also hampered by the necessity to make major simplifications in the simulated system. However, new techniques based on massively parallel computers and increased single-processor capabilities have now made 3D simulations of realistic flow problems feasible. This development is further augmented by the recent introduction of new flow-simulation algorithms (in particular the lattice-gas and lattice-Boltzmann methods) that are very well suited for parallel computing. There is hope, that in the future numerical simulations can be used to radically improve our understanding of complicated flow phenomena.

5.2 Previous studies with lattice-gas and lattice-Boltzmann methods

When the lattice-gas method was introduced, it was soon realized that it would be very useful for simulating fluid flow in porous media. In Ref. [103] (of 1987), which is one of the earliest studies, the validity of Darcy's law Eq. (5.1) was verified in a 2D system constructed of randomly placed solid points. In the classical paper Ref. [88] (of 1988), simulations in a complex 2D medium were performed. Reference [104] (of 1989) is among the first 3D studies. The aim of this paper was to demonstrate the validity of the lattice-Boltzmann model in simulating fluid flow in complex 3D geometries.

Several authors have used lattice-gas and lattice-Boltzmann methods to study fluid flow in various 2D porous media. In these studies the medium has been composed of overlapping rectangles, overlapping and non-overlapping spheres, crusiformed obstacles, or has been a 2D digitized image of an etched glass micromodel [91, 92, 105, 106, 107].

In Refs. [14, 108, 109] various 3D simulations have been reported. In Ref. [108] fluid flow through an array of randomly placed spheres was stud-

ied, and the validity of the Kozeny law, Eq. (5.2) below, for this particular medium was clearly demostrated. In Ref. [109] fluid-flow simulations in a 3D medium generated by a fractal generator were reported. In Ref. [110] fluid flow through a digital image of clay soil was studied. The simulated permeability was found to be consistent with experimental values. It was also found that the Kozeny-Carman equation did not provide a very succesful estimate for the permeability of this particular medium. In Ref. [14] fluid flow through a digital image of Fointainebleau sandstone was studied. The simulated permeabilities were found to compare well with experimental data. In the last reference statistical fluctuations of permeability were also discussed.

5.3 Permeability of a porous substance

In theoretical and experimental work on fluid flow in porous media it is typically attempted to find functional correlations between the permeability and some other macroscopic properties of the porous medium [22]. Among the most important of such properties are the porosity ϕ and the specific surface area S, which give the ratios of the total void volume and the total interstitial surface area to the bulk volume, respectively. Another useful characteristics of porous media is the tortuosity τ, which has been introduced to account for the complexity of the actual microscopic flow paths through the substance [II, 17, 22]. Tortuosity can be defined as the ratio of a (properly weighted) average length of microscopic flow paths to the length of the system in the direction of the macroscopic flux [II].

Simple dimensional analysis suggests that the permeability of a porous medium is of the form $k = f(\phi, \tau)/S^2$, where $f(\phi, \tau)$ is a dimensionless function of ϕ and τ. Various simplified models can be used to find suitable candidates for f. The Darcy's law, Eq. (5.1), can easily be derived within the simple capillary theory by Kozeny, in which the porous medium is envisaged as a layer of solid material with straight parallel tubes of a fixed cross-sectional shape intersecting the sample. Within this model, the permeability is explicitely given as [17, 22, 24, 25]

$$k = \frac{\phi^3}{cS^2}, \tag{5.2}$$

where c is the Kozeny coefficient that depends on the cross-section of the capillaries. For cylindrical capillaries, $c = 2$. The simplest way to introduce

tortuosity in the capillary model is to allow the tubes to be inclined in such a way that the axes of the capillaries form a fixed angle θ with the normal of the surface of the material (while the azimuthal angle of the tubes is randomly distributed). In this case permeability becomes

$$k = \frac{\phi^3}{c\tau^2 S^2}, \tag{5.3}$$

where $\tau = 1/\cos\theta$ is the tortuosity of the medium which can be given in terms of the tube length L_e and the thickness of the medium L as

$$\tau = L_e/L. \tag{5.4}$$

(Some authors prefer to define tortuosity as $\tau = (L_e/L)^2$ or as the inverses of these two definitions [22, 111]. Here, we shall use definitions analogous to Eq. (5.4). Thus, for the tortuosity defined here, $\tau \geq 1$.) In next section we shall discuss the concept of tortuosity in more detail.

Equations (5.2) and (5.3) are perhaps the most widely used expressions for the permeability of a porous medium. Many porous media conform to them quite well, although quantitative agreement should not generally be expected. For systems composed of randomly placed obstacles, *e.g.*, permeability behaves for high porosities ($\phi \to 1$) as $1/(1-\phi)$, and the Kozeny model is not valid.

While considering flow through porous medium, only the interconnected pores are of interest, as the occluded pores (pores not connected to the main void space) do not contribute to the flow. (The term porosity is sometimes used to include the interconnected pore space only.) The dead-end pores are another type of pores that contribute very little to the flow. These pores belong to the interconnected pores, but, owing to their geometry, no global pathlines intersect them. The occluded pores and the dead-end pores form the non-conducting pore space of the medium. The effective porosity ϕ_{eff} of a porous medium can be defined as the ratio of the volume of the conducting pores to the total volume of the medium.

A common method of constructing models of porous media is to place solid obstacles in a two- or three-dimensional test volume [23]. The properties of the medium are determined by the shape, size and number of the obstacles, and by the distribution of the obstacles within the volume. In such "materials" with high porosity, all of the void space usually contributes to flow through it. The effective porosity of the medium is then equal to porosity. In contrast with this, for low-porosity materials, a large part of

the total void space may be non-conducting. For such media the effective porosity may therefore be significantly smaller than the geometrical porosity. At the percolation threshold, defined as the point $\phi = \phi_c$ where the medium becomes completely blocked, permeability and effective porosity both vanish. It is therefore clear that for porous media for which the percolation threshold appears at a finite porosity ϕ_c, the Kozeny equation, as given by Eqs. (5.2) or (5.3), is not valid for $\phi \to \phi_c$.

The simplest way to modify Eqs. (5.2) and (5.3) to include the effect of non-conducting pores is to replace the porosity ϕ with the effective porosity ϕ_{eff} (notice that in simple capillary models $\phi_{\text{eff}} = \phi$). We thus get [III]

$$k = \frac{\phi_{\text{eff}}^3}{cS^2}, \tag{5.5}$$

or

$$k = \frac{\phi_{\text{eff}}^3}{c\tau^2 S^2}. \tag{5.6}$$

Notice that all three quantities ϕ_{eff}, τ and S are functions of porosity.

At this point, we shall not try to further substantiate Eqs. (5.5) and (5.6). Instead, we shall below compare the results of lattice-gas simulations with permeabilities given by Eqs. (5.2), (5.3), (5.5) and (5.6).

5.4 Tortuosity of flow in porous medium

A common characteristics of any material transport in porous media, such as fluid flow or electric current, is that the actual path followed by the transported entity is microscopically very complicated, or "tortuous" [17, 22, 25, 111] (examples of such paths are shown in Fig. 5.1). The concept of tortuosity is often introduced in the context of solving the closure problem for transport in porous media, *i.e.*, in deriving the macroscopic transport equations in terms of averaged quantities alone.

As a physical quantity, tortuosity can be defined in various ways. Perhaps the most intuitive and straightforward definition is that of the ratio of the average length of true flow paths to the length of the system in the direction of macroscopic flux (see Fig. 5.2a). Notice that by this definition, tortuosity depends not only on the microscopic geometry of the pores, but also on the transport mechanism under consideration.

Tortuosity could also be defined without reference to a specific transport mechanism. This could be done for example by considering the shortest continuous paths between any two points within the pore space [112] (see

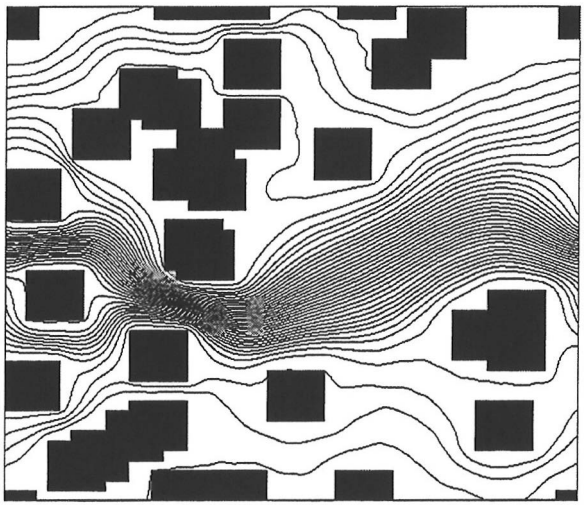

Figure 5.1: Flow lines through a two-dimensional random porous medium.

Fig. 5.3b). The advantage of this definition is that the tortuosity parameter thus defined will exclusively characterize the porous substance itself. When considering tortuosity in the context of transport phenomena, it seems quite more natural, however, to utilize the flux associated with the actual transport mechanism in the definition of tortuosity.

Moreover, it is possible to define tortuosity even without a direct reference to the lengths of the transport paths by considering the local deviations in the direction of the microscopic flux from the direction of the mean flux (see Fig. 5.3a). (This approach will be discussed in some detail below.)

We saw above, how the concept of tortuosity is introduced into permeability by using a simple inclined tube capillary model (see Eqs. (5.3) and (5.4)). For flow in random porous media, one can replace the "tube length" L_e by the average length of the flow paths of a fluid particle through the sample. At least two possible alternatives for taking this average can be considered [22]. One may average over the actual lengths of the *flow lines themselves*, disregarding thereby the fact that fluid particles move along these flow lines at different velocities (see Fig. 5.2a). Another way of averaging is over the lengths of the *flow lines of all fluid particles* passing through a given cross-section during a given period of time (see Fig. 5.2b). This leads to flux weighted averaging. The first alternative is suitable at least for piston-like flows, such as molecular diffusion and electric currect [22]. The

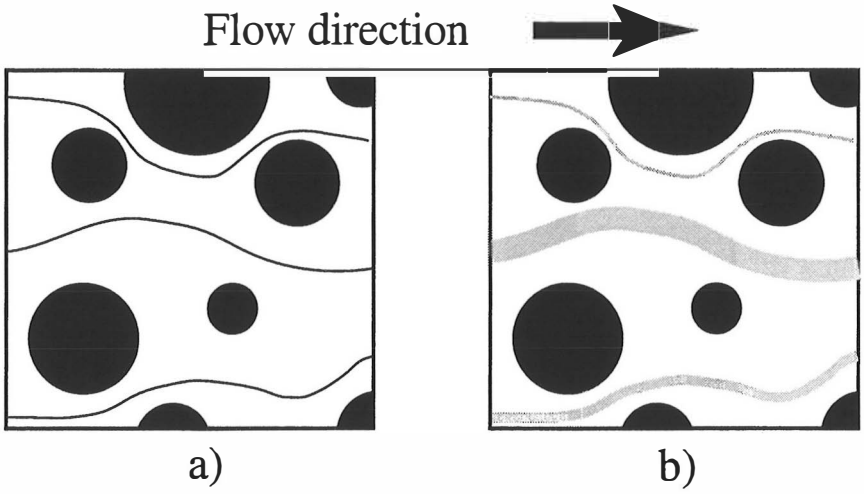

Figure 5.2: Different ways of defining the tortuosity. Figure a): Tortuosity calculated as an average over the lengths of all pathlines. Figure b): Tortuosity calculated as an average over the lengths of all pathlines weighted with the related flux.

latter alternative appears more natural when fluid flow in porous media is considered.

In order to gain more insight into the definition (or definitions) of tortuosity of flow in porous media, we consider a solid material of thickness L, intersected by N cylindrical capillaries per unit transverse area. We assume that the capillaries are straight and of equal radius R, but allow for a randomly varying angle between them and the x axis, which is perpendicular to the surfaces of the material. For the i:th capillary of length L_i we define, in acordance with Eq. (5.4), $\tilde{\tau}_i = L_i/L$. Next, flow through the capillaries is induced by applying a pressure difference Δp across the sample. Solving the Navier-Stokes equation for each capillary separately, we obtain after some algebra the following suggestion for the tortuosity of porous medium [II]:

$$\tau^2 = \tau_1 \tau_{-1}, \tag{5.7}$$

where

$$\tau_1 = \frac{\int_V \tilde{\tau} v dV}{\int_V v dV} \tag{5.8}$$

$$1/\tau_{-1} = \frac{\int_V \frac{1}{\tilde{\tau}} v dV}{\int_V v dV}. \tag{5.9}$$

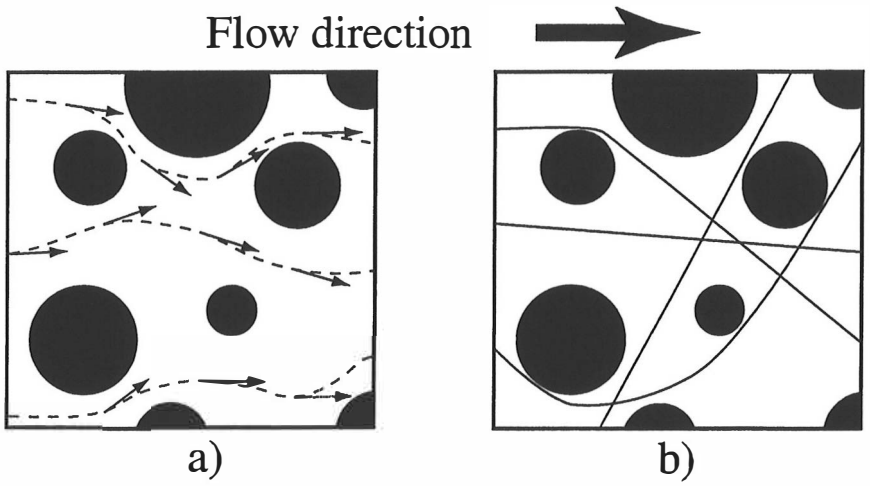

Figure 5.3: Different ways of defining the tortuosity. Figure a): Tortuosity calculated from the fluctuations of the local velocity field around the direction of the average flux. Figure b) Tortuosity calculated from the shortest continuous paths between points in the void space.

Above V is the volume of the porous sample, $v = |\mathbf{v}(\mathbf{r})|$ is the velocity of the fluid at point $\mathbf{r}$, and $\tilde{\tau} = \tilde{\tau}(\mathbf{r})$ is the ratio of the length of the flow line passing through the point $\mathbf{r}$ to the thickness of the sample. ($\tilde{\tau}$ and v are defined to be zero inside the solid phase.)

The tortuosity factor as determined by Eq. (5.8) can be interpreted as the average of the relative lengths of the flow lines of all fluid elements (with a fixed volume) passing through a given cross-section during a given period of time. The latter definition Eq. (5.9) corresponds to the average of inverse lengths of the same flow lines.

Equations (5.7) through (5.9) do not, however, provide the only way of generalising the results of capillary model to random media. For example, in the case of capillary systems, the tortuosity factor τ_{-1} of Eq. (5.9) is in fact equal to the ratio

$$\tau_v \equiv \frac{\langle |\mathbf{v}| \rangle}{\langle v_x \rangle}, \tag{5.10}$$

where $|\mathbf{v}|$ is the absolute value of the local flow velocity, v_x is the x component of that velocity, and $\langle\ \rangle$ denotes spatial average over the pore space. Notice that Eq. (5.10) is reminiscent of the hypothesis made by Carman in Ref. [25] that $(L_e/L) = \bar{V}/\bar{u}_e$, where $\bar{V}$ is the average tangential velocity in a tortuous

capillary, L_e is the length of that capillary, $\bar{u}_e$ is the mean value of the projection of flow velocity on the straight line connecting the two ends of the capillary, and L is the length of that line. According to Eq. (5.10), τ_v is solely determined by fluctuations of the local flow field around the direction of the average flux, and has no direct connection with the length of the actual flow paths.

In deriving the above results, we assumed that the radius of the capillaries is fixed while their lengths may vary. The results are, however, valid also in the case of varying capillary radii, provided that these and the lengths of the capillaries are uncorrelated.

Yet another possibility, which may be encountered in other kinds of models, is to define the tortuosity as an average of the lengths of flow lines squared [22, 111]. Analogously to Eqs. (5.8) and (5.9), we may then define

$$(\tau_2)^2 = \frac{\int_V v\tilde{\tau}^2 dV}{\int_V v dV} \tag{5.11}$$

$$\frac{1}{(\tau_{-2})^2} = \frac{\int_V v\frac{1}{\tilde{\tau}^2} dV}{\int_V v dV}. \tag{5.12}$$

Thus, tortuosity is not uniquely defined, and the preferred definition must depend on the context and on the model being used. Our simulations in 2D random porous medium suggest, however, that the model dependence can be quite small, at least for a two-dimensional flow at relatively high porosities [II]. The smallness of the differences between the numerical values of this quantity, arising from its various plausible definitions, seems to indicate that tortuosity indeed is a useful concept.

5.5 Specific surface area, tortuosity, and effective porosity of a 2D porous medium

In order to effectively compare the different models of permeability with results of lattice-gas simulations, it is beneficial to first cast the Eqs. (5.2), (5.3), (5.5) and (5.6) into explicit functions of porosity ϕ alone [III]. To do this, we have to find the dependence on the porosity ϕ of the specific surface area S, the tortuosity τ and the effective porosity ϕ_{eff}. We choose as our model medium a simple 2D model in which rectangles of equal size are placed randomly with unrestricted overlap in a two-dimensional volume (see Fig. 5.5). Although such a model may be considered somewhat artificial, it

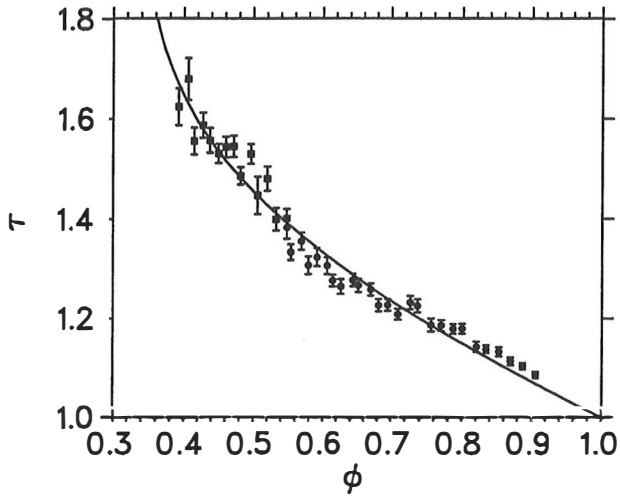

Figure 5.4: The simulated tortuosity τ as a function of porosity ϕ [III]. The error bars include the statistical errors in tortuosity only. The solid line is a fit to the simulated points by Eq. (5.14).

nevertheless captures much of the geometrical complexity of natural porous media.

For the specific surface area S, the following simple and appealing analytic relation holds in our model medium:

$$S = -\frac{2}{R_0}\phi \ln \phi. \tag{5.13}$$

Here $R_0 = A_0/L_p$ (A_0 is obstacle-surface area and L_p is its perimeter) is the hydrodynamic radius of the obstacles.

The porosity dependence of tortuosity τ and effective porosity ϕ_{eff} are analytically very difficult to find. For this reason we have derived them from direct lattice-gas simulations. The simulated values of tortuosity τ are shown in Fig. 5.4 as a function of porosity ϕ. Also shown in this figure is a fit to the simulated values using a function of the form

$$\tau = 1 + a\frac{(1-\phi)}{(\phi - \phi_c)^m}, \tag{5.14}$$

with the values of the fitting parameters being $a = 0.65$ and $m = 0.19$. The expression Eq. (5.14) has been chosen such that tortuosity is a monotonously decreasing function of porosity (at $\phi > \phi_c$) and diverges at the percolation

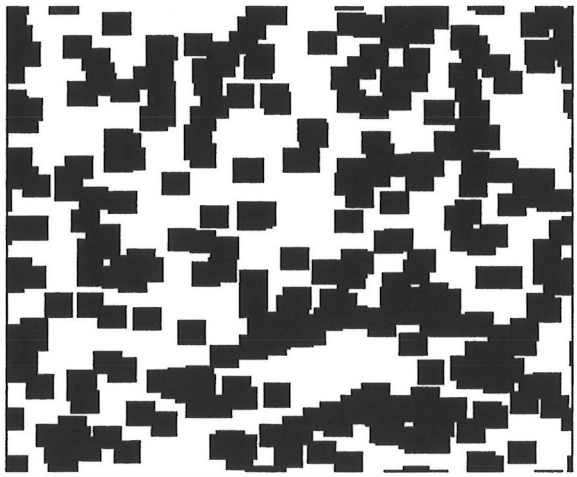

Figure 5.5: A porous sample composed of 300 rectangles and having a porosity of $\phi = 0.47$, and a dimensionless specific surface area of $S = 0.69$.

threshold ϕ_c [23]. For the present system the percolation threshold is $\phi_c = 0.33$ [113].

The conducting pore space (white regions) of the porous sample shown in Fig. 5.5 is shown in Fig. 5.6. The (geometrical) porosity of the sample is $\phi = 0.47$ while the effective porosity in this particular case is $\phi_{\text{eff}} = 0.40$.

In Fig. 5.7 we show the simulated values of the effective porosity as a function of porosity. The solid line shown in Fig. 5.7 is a fit to the simulated points by

$$\phi_{\text{eff}} = ax^3 - (2a + \phi_c)x^2 + (a + 1 + \phi_c)x, \tag{5.15}$$

where $x = (\phi - \phi_c)/(1 - \phi_c)$. The fitted value of the parameter a is $a = 0.3$. The expression Eq. (5.15) is simply the most general third order polynomial in which the natural constraints, $\phi_{\text{eff}} = \frac{d\phi_{\text{eff}}}{d\phi} = 1$ at $\phi = 1$, and $\phi_{\text{eff}} = 0$ at $\phi = \phi_c = 0.33$, have been implemented. With the given values of ϕ_c and a, this expression also fulfills the condition that $\phi_{\text{eff}} \leq \phi$ for all $\phi \leq 1$. We emphasize that the true functional form of ϕ_{eff} as a function of ϕ is not known. Expressions other than Eq. (5.15) can also be found which would give a good quantitative fit to the results of the present simulations. As an example we give the expression

$$\phi_{\text{eff}} = 1 - \frac{\ln \phi}{\ln \phi_e}, \tag{5.16}$$

Figure 5.6: The conducting pore space of the porous sample shown in Fig. 5.5 corresponding to an effective porosity $\phi_{\text{eff}} = 0.40$.

which gives a good quantitative fit to the simulated results, but, with porosities higher than 0.8, the expression produces ϕ_{eff} larger, if only very slightly, than ϕ. It thus fails to give a qualitatively correct behaviour in this porosity region.

5.6 Permeability of a 2D porous medium

The permeabilities for the 2D random porous medium simulated with the lattice-gas method are shown in Fig. 5.8 [III]. Also shown are the predictions given by the permeability expressions, Eqs. (5.2), (5.3), (5.5) and (5.6). Here S, τ and ϕ_{eff} are given by Eqs. (5.13), (5.14) and (5.15), respectively, with the theoretical value $\phi_c = 0.33$. (The Kozeny coefficient c was used as the fitting parameter.) The permeabilities were made dimensionless by dividing with the hydraulic radius R_0 squared. For expressions Eqs. (5.2) and (5.3) (curves 1 and 2 in Fig. 5.8), fits to all of the data points were clearly unsatisfactory. Therefore, fits were made, instead, in a narrow porosity region at mid-porosities, where these formulae seem to give a qualitatively correct porosity dependence for the simulated permeabilities. For expressions Eqs. (5.5) and (5.6) (curves 3 and 4 in Fig. 5.8) fits were made to all data points.

As can be seen from Fig. 5.8, the porosity region in which the Kozeny

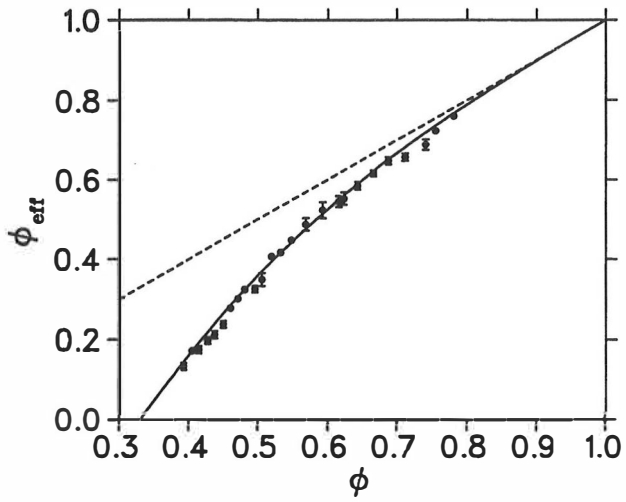

Figure 5.7: The simulated effective porosity ϕ_{eff} as a function of porosity ϕ. The solid line is the fit by Eq. (5.15), and the dotted line is the curve $\phi_{\text{eff}} = \phi$. The error bars include only the statistical errors of the simulations.

equation in its basic form, Eq. (5.2), is adequate for this particular system, is quite narrow. Taking into account the effect of tortuosity by Eq. (5.3) improves the fit only slightly. The result is significantly improved only by introducing the effective porosity, Eq. (5.5), and an even better result is obtained by Eq. (5.6) in which the tortuosity and effective porosity are both included.

The fitted values of the Kozeny coefficient c were 8.2, 6.5, 10.4 and 5.8 for Eqs. (5.2), (5.3), (5.5) and (5.6), respectively. This is in good agreement with various models and measurements found in the literature, where typically values for the Kozeny coefficient c are reported in the range from 2 to 12 [17, 19, 22].

It is evident that the permeability of two-dimensional random porous media is very much affected by restrictions on flow caused by narrow passages and dead-end pores. A 3D simulation of fluid flow through a bed of penetrable spheres was earlier made in Ref. [108] in which good quantitative agreement with the Kozeny equation Eq. (5.2) was obtained down to $\phi \approx 0.1$, below which there was still a good qualitative fit. The difference between these and the present results is caused by the weaker tendency to form occluded pores, and the much lower value of the percolation threshold ϕ_c of the three-dimensional system used in Ref. [108] in comparison with the

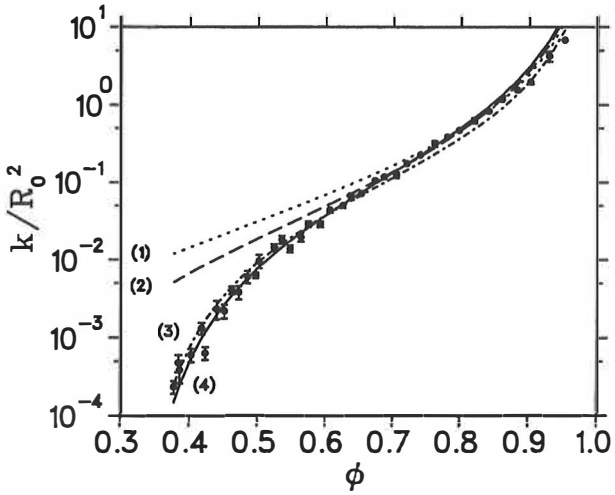

Figure 5.8: The simulated dimensionless permeability k/R_0^2 of the porous system as a function of porosity ϕ. The error bars show the statistical errors of simulations. The curves 1 – 4 show the predictions given by the permeability expressions Eqs. (5.2), (5.3), (5.5) and (5.6), respectively.

two-dimensional system used here. Therefore, for such a three-dimensional system, effective porosity may be close to the geometrical porosity also for rather low values of the porosity. It may well be, however, that the actual structure of the pore space available for flow plays an important role also in three dimensions. It remains to be seen, *e.g.*, if effective porosity becomes important for such three-dimensional porous structures in which the percolation threshold is relatively high.

5.7 Permeability of 3D random fibre webs

In many natural and man-made porous media the porous structure is fibrous. Despite of the numerous experimental and theoretical studies (see Ref. [20] for a comprehensive review), permeability characteristics of disordered fibrous porous media are still poorly understood. The existing numerical studies include those on fluid flow through random arrays of parallel cylinders, suspension of prolate spheroids, and three-dimensional regular fibre networks [114, 115, 116], which all neglect the disorder typical of real 3D fibre webs. Recently, 3D fluid-flow simulations have been performed through randomly placed cylinders with relatively high porosities [117].

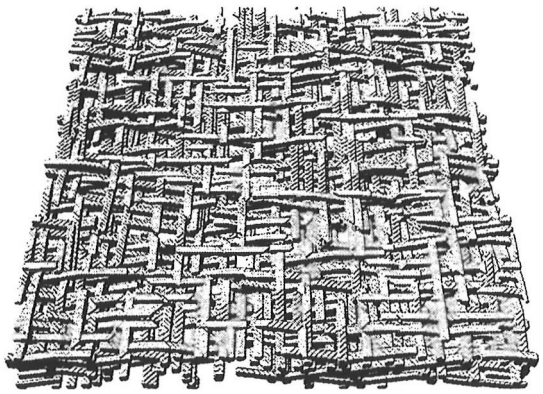

Figure 5.9: A fibre-web sample constructed with the growth algorithm. The web porosity is $\phi = 0.83$.

We have performed three-dimensional *ab initio* lattice-Boltzmann simulations of creeping flow through large random fibre webs [I]. The model web structures were constructed using a recently introduced growth algorithm [118]. Within this algorithm, fibre webs are grown by sequential random deposition of flexible fibres of rectangular cross-section on top of a flat substrate. Each fibre is randomly oriented either in the x or y direction, and is then let to fall in the negative z direction until it makes its first contact with the underlying structure. After this it is bent downwards without destructing the structure. Periodic boundary conditions are used in x and y directions. In Fig. 5.9 we show a sample created by this algorithm [I]. It is evident that the produced structures closely resemble those of *e.g.* paper and non-woven fabrics (restriction to the x and y directions can be relaxed and does not play an important role here).

Simulations were performed using the 19-link lattice-BGK model. Fibre dimensions were $w_F \times w_F \times 20w_F$, while sample dimensions were $80w_F \times 80w_F \times 10w_F$ (here w_F is the fibre thickness in lattice units). The web porosities ϕ ranged from 0.42 to 0.95. The fibre thickness w_F varied from 5 to 10 lattice points depending on the porosity of the sample. For these discretizations, the finite-size errors of the simulated permeabilities were estimated to be less than 15%. (We have discussed the finite-size effects related to these simulations in Chapter 4 above.) When 32-bit floating point

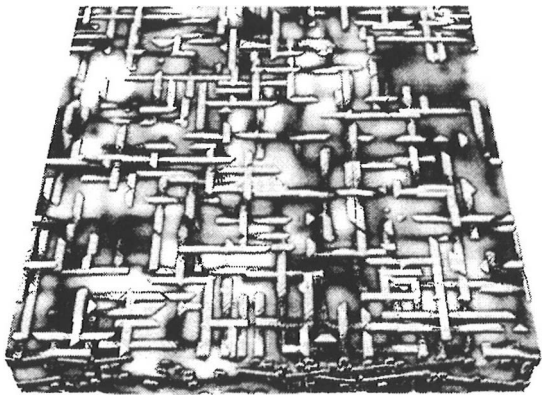

Figure 5.10: The velocity field of fluid flow through the fibre web shown in Fig. 5.9. White color indicates high fluid velocity.

numbers were used, the larger web required 5.4 GByte of core memory. The simulations were therefore carried out using 64 nodes (300 MHz CPUs with 128 MByte of memory) on a Cray T3E system. The saturation times were decreased by using the iterative momentum relaxation (IMR) method. The required CPU time was typically between 1 and 4 hours.

In Fig. 5.10 we show the simulated stationary velocity field for a flow in the z direction through the highly inhomogeneous sample shown in Fig. 5.9. It is evident that there are large fluctuations in the velocity field reflecting the variations in the local porosity of the sample. The average velocity $\langle v_z \rangle$ shown in Fig. 5.10 is $\langle v_z \rangle = 0.00142$, with a standard deviation of $\Delta v_z = 0.00128$. These fluctuations, which are inherent in random porous structures, will affect the permeability, except at very high porosities, such that it is expected to become higher than that for regular arrays of pores [20]. This effect will be seen in the results given below.

In Fig. 5.11 we show the simulated dimensionless permeability of the random fibre web as a function of its porosity. (The permeabilities have been made dimensionless by dividing them with $a = w_F/2$ squared.) In this figure solid triangles denote the simulated values. It is evident that there are two distinct features in the simulated $k(\phi)$ curve. Firstly, it seems to diverge as expected when $\phi \to 1$, and, secondly, k seems to be an exponential function of ϕ for a rather wide range of ϕ: $0.42 \leq \phi \leq 0.85$.

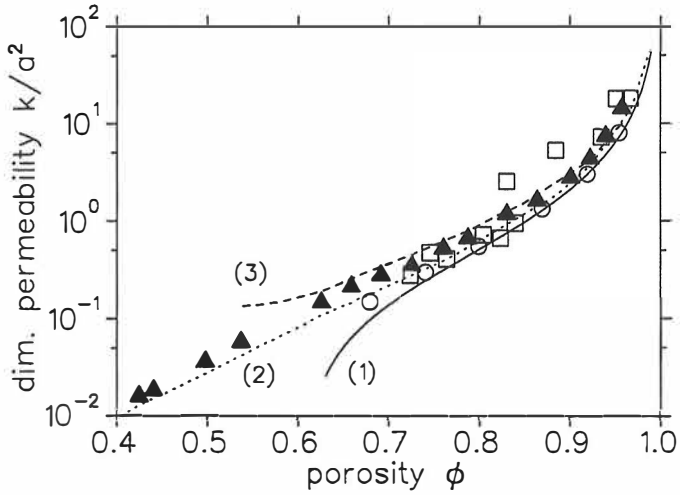

Figure 5.11: The simulated dimensionless permeability k/a^2 as a function of porosity (black triangles). Open squares and circles show the experimental results for fibrous filters [20] and compressed fibre mats [18, 20], respectively. Curve (1) is the analytical result for a cubic lattice given in Ref. [20], curve (2) is the numerical result for an fcc lattice from Ref. [116], and curve (3) shows the result of a fit by the Kozeny-Carman relation, Eq. (5.2).

A fit of the form $k/a^2 = \text{constant} \cdot (1-\phi)^{-\mu}$ to the last five points with highest porosities gives $\mu = 1.92$. This results shows that, even for these rather high porosities $\phi \leq 0.96$, the system is not in the true asymptotic region for which $\mu = 1$. The reason for this is that the fibres of the web are still close enough to each others so that there are significant hydrodynamic interactions between them. On the other hand, the simple capillary-tube model by Kozeny and Carman [22] gives $k/a^2 \propto \phi^3(1-\phi)^{-2}$ in this limit so that, as expected, the simulated behaviour of $k(\phi)$ is in rather good agreement with this model with high porosities.

A fit of the form $\ln(k/a^2) = A + B\phi$ to the rest of the simulated points gives $A = -8.53$, $B = 10.4$, with a very high correlation between the simulated points and the fitted curve. So far there have been no analytic results which would have produced this kind of exponential behaviour at intermediate porosities. It will not hold near the percolation threshold at which permeability vanishes. This critical region is however beyond the present computational capabilities.

It is evident from Fig. 5.11 that experimental results [18, 20] (denoted

by open circles and squares) conform well with the simulated points. The model web used here thus captures the essential features of the fibrous filters and compressed fibre mats used in the experiments.

Also shown in Fig. 5.11 are three curves which are results of previous analytical [20] (curve (1)), numerical [116] (curve (2)) and semi-empirical [18, 19, 22] (curve (3)) considerations. Curve (1) is given by $k/a^2 = 3[-\ln(1-\phi) - 0.931 + O(1/\ln(1-\phi))]/20(1-\phi)$, an expression obtained for a cubic lattice model [20], and curve (2) results from a numerical solution [116] for the Stokes flow in a face-centered-cubic (fcc) array of fibres. Both these curves are below the simulated points, especially for decreasing porosity. Notice that the fcc result also follows an exponential law at intermediate porosities.

Curve (3) is given by the Kozeny-Carman expression Eq. (5.2) where the following empirical fit to measured permeabilities has been used [18, 19]: $c = 3.5\phi^3[1 + 57(1-\phi)^3]/(1-\phi)^{\frac{1}{2}}$. We have used this expression to get the curve (3) from Eq. (5.2). The specific surface area S was determined from the surface area of the (straight) fibres used to construct the web by subtracting the area of the interfibre contacts. Because of bending of the fibres this expression gives a lower bound for S, and curve (3) is expected to overestimate the permeability. This is indeed what happens (see Fig. 5.11).

Encouraged by the exponential behaviour at intermediate porosities of $k(\phi)$, we have made an interpolation formula that connects this behaviour with the right asymptotics in the limit $\phi \to 1$. We find that the expression

$$k/a^2 = A[e^{B(1-\phi)} - 1]^{-1} \tag{5.17}$$

with $A = 5.55$, $B = 10.1$, fits all the simulated points very well.

These results clearly demonstrate that the combination of lattice-Boltzmann method and parallel computing facilitates simulations of realistic fluid-dynamical problems of great complexity. We believe that this approach will be very fruitful for modelling and simulating many complex fluid-dynamical systems.

Chapter 6

Summary

In this work, we have used the lattice-gas and lattice-Boltzmann methods for solving several problems of creeping flow of a Newtonian fluid through 2D and 3D random porous media. We have found numerical correlations between the specific surface, tortuosity, effective porosity, permeability and porosity of a 2D porous medium. We have demonstrated that although fluid tortuosity is not uniquely defined as a physical quantity, its model dependence can be quite small, and the tortuosity can indeed be a useful parameter in describing fluid transport in complex structures of real porous materials. Also, we have suggested an improved Kozeny-Carman law that takes into account the effect of the nonconducting porosity of the medium. This expression has been found to fit very well the simulated 2D permeabilities, whereas the traditional permeability expressions have clearly been found to fail for low porosities of the considered 2D medium. These results suggest that the permeability of a porous medium can be appreciably affected by restrictions on flow caused by narrow passages and dead-end pores, at least for such porous structures for which the percolation threshold is relatively high. We have also solved the permeability of a large random 3D fibre web as a function of its porosity in a large porosity range. The simulation results have been found to be in excellent agreement with experimental data. Also, an exponential dependence on porosity of permeability has been found to be a generic feature of fibrous porous materials in a wide range of porosities, independent of whether they are random or not.

We have also discussed many practical problems related to the lattice-gas and lattice-Boltzmann methods, and have *e.g.* demonstrated that even the simplest realizations of these methods (*i.e.* the bounce-back rule and body

force) can be used to get good quantitative hydrodynamics. We have introduced an improved relaxation scheme, the Iterative Momentum Relaxation (IMR) method, and a new parallelization strategy based on the Orthogonal Recursive Bisection (ORB) method, which both can considerably speed up the lattice-gas and lattice-Boltzmann simulations.

These results clearly demonstrate that the lattice-gas and lattice-Boltzmann methods can provide promising alternative approches to traditional computational fluid dynamics. Their most important property is the simplicity with which models for many complex systems can be constructed. So far, successful implementations of these methods have included *e.g.* multiphase flows, suspension flows and flows in complex geometries. All these problems have been difficult to simulate with conventional methods. Another important property is the inherent spatial locality of their updating rules, which makes these methods ideal for parallel processing. Grid generation has often been the most difficult part in solving a fluid-dynamical problem. In the lattice-gas and lattice-Boltzmann methods a uniform lattice is used, and they can thus be easily and quickly applied to new geometries. Also, time-dependent simulations can relatively easily be carried out, as no time is lost for remeshing. Moreover, these methods spontaneously generate hydrodynamic instabilities. They could thus be useful for simulating fluid flow at moderately large Reynolds numbers.

The lattice-gas and lattice-Boltzmann methods have also some drawbacks. At large Reynolds numbers they meet the same problem as the more conventional methods: in a fully turbulent flow wave lengths of all scales are present, and the solution of the problem would require enormous simulation lattices. In many practical applications the uniformity of the lattice is a problem, as a sufficiently high computational accuracy would necessitate very big lattices. However, new models including a local grid refinement may remove this problem in the near future. Also, some basic features of the methods, such as boundary conditions and models for finite-temperature systems, are still under development.

In the near future, the traditional continuum methods will surely remain the most important way for doing computational fluid dynamics. However, in many fields the lattice-gas and lattice-Boltzmann methods will facilitate simulations of many realistic fluid-dynamical problems of great complexity.

Bibliography

[I] Publication I of this thesis.

[II] Publication II of this thesis.

[III] Publication III of this thesis.

[IV] Publication IV of this thesis.

[V] Publication V of this thesis.

[1] R. Fox, and A. McDonald, *Introduction to fluid mechanics* (John Wiley & Sons, Singapore, 1985).

[2] Chris Teixeira, *Continuum limit of lattice-gas fluid dynamics* (PhD Thesis, MIT, 1992).

[3] U. Frisch, B. Hasslacher, and Y. Pomeau, Phys. Rev. Lett. **56**, 1505 (1986).

[4] U. Frisch, D. d'Humiéres, B. Hasslacher, P. Lallemand, Y. Pomeau, and J.-P. Rivet, Complex Syst. **1**, 649 (1987).

[5] D.H. Rothman, and S. Zaleski, Rev. Mod. Phys. **66**, 1417 (1994).

[6] D. H. Rothman, and S. Zaleski, *Lattice-gas cellular automata* (Cambridge University Press, Cambridge, 1997).

[7] R. Benzi, S. Succi, and M. Vergassola, Phys. Rap. **222**, 145 (1992).

[8] B. Dubrulle, U Frish, M. Henón, and J.-P. Rivet, J. Stat. Phys. **59**, 1187 (1990).

[9] D.V. van Coevorden, M. H. Ernst, R. Brito, and J. A. Somers, J. Stat. Phys. **74**, 1085 (1994).

[10] G. McNamara, and G. Zanetti, Phys. Rev. Lett. **61**, 2332 (1988).

[11] F.J. Higuera, and J. Jimenez, Europhys. Lett. **17**, 668 (1989).

[12] F. Higuera, S. Succi, and R. Benzi, Europhys. Lett. **9**, 345 (1989).

[13] Y.H. Qian, D. d'Humiéres, and P. Lallemand, Europhys. Lett. **17**, 479 (1992).

[14] B. Ferréol, and D. H. Rothman, Transport in Porous Media **20**, 3 (1995).

[15] A. J. C. Ladd, J. Fluid. Mech. **271**, 285 (1994); ibid. **271**, 311 (1994).

[16] H. Darcy, *Les Fontaines Publiques da la Ville de Dijon* (Dalmont, Paris, 1856).

[17] A. Scheidegger, *The physics of flow in porous media* (The Macmillian company, New York, 1957).

[18] W. L. Ingmanson, B. D. Andrews, and R. C. Johnson, TAPPI **42**, 840 (1959).

[19] S. T. Han, Pulp Paper Mag. Can. **70**, T134 (1969).

[20] G. W. Jackson, and D. F. James, Can. J. Chem. Eng. **64**, 364 (1986).

[21] See S. Kostek, L. M. Schwartz, and D. L. Johnson, Phys. Rev. B **45**, 186 (1992); A. H. Thompson, S. W. Sinton, S. L. Huff, A. J. Katz, R. A. Raschke, and G. A. Gist, J. Appl. Phys. **65**, 3259 (1989); D. L. Johnson, D. L. Hemmick, and H. Kojima, J. Appl. Phys. **76**, 104 (1994), and references therein.

[22] J. Bear, *Dynamics of Fluids in Porous Media* (Dover, New York, 1972).

[23] M. Sahimi, *Flow and Transport in Porous Media and Fractured Rock* (VCH, Weinheim, 1995).

[24] Kozeny, Ber. Wien Akad. **136**a, 271 (1927).

[25] P. Carman, Trans. Inst. Chem. Eng. **15**, 1550 (1937).

[26] J. Cushman, *Dynamics of fluids in hierarchical porous media* (Academic press, San Diego, 1990).

[27] N. Martys, and H. Chen, Phys. Rev. E **53**, 743 (1996).

[28] S: Wolfram, J. Stat. Phys. **45**, 471 (1986).

[29] B. Chopard, and M. Drotz, *Cellular automata modelling of physical systems* (Lecture notes, University of Geneva, 1996).

[30] G. Zanetti, Phys. Rev. A **40**, 1539 (1989).

[31] L. Kadanoff, G. McNamara, and G. Zanetti, Phys. Rev. A **40**, 4527 (1989).

[32] J. Hardy, Y. Pomeau, and O. de Pazzis, Phys. Rev. A **13**, 1949 (1976).

[33] N. Margolus, T. Toffoli, and G. Vichniac, Phys. Rev. Lett. **56**, 1694 (1986).

[34] K. Huang, *Statistical mechanics* (New York, 1967).

[35] D. d'Humiéres, and P. Lallemand, Europhys. Lett. **2**, 291 (1986).

[36] J. Olson, private communication.

[37] G. Strumolo, and V. Babu, Phys. World august 1997, 45 (1997).

[38] J. Olson, *Two-fluid flow in sedimentary rock: complexity, transport and simulation* (PhD thesis, MIT, 1995).

[39] J. Olson, and D. Rothman, J. Stat. Phys. **81**, 199 (1995).

[40] C. Appert, J. Olson, D. Rothman, and S. Zaleski, J. Stat. Phys. **81**, 181 (1995).

[41] I. Halliday, and C. Care, Phys. Rev. E. **53**, 1602 (1996).

[42] J. Wells, D. Janecky, and B. Travis, Physica D **47**, 115 (1991).

[43] J. Weimar, D. Dab, J.-P. Boon, and S. Succi, Europhys. Lett. **20**, 627 (1992).

[44] S. Chen, P. Dawson, D. Doolen, D. Janecky, and A. Lawniczak, Computers Chem. Engng. **19**, 617 (1995).

[45] E. Flekkøy, J. Feder, and T. Jøssang, J. Stat. Phys. **68**, 515 (1992).

[46] A. Ladd, and D. Frenkel, Phys. Fluids. A **2**, 1921 (1990).

[47] A. Ladd, Dissipative and fluctuating hydrodynamic interactions between suspended solid particles via lattice-gas cellular automata, pp. 481-504 in M. Mayer, and V. Pontikis, *Computers in simulation in material science* (Kluver Academic Publishers, Netherlands, 1991).

[48] S. Chen, M. Lee, K. Zhaq, and G. Doolen, Physica D **37**, 43 (1989).

[49] Y. Chen, H. Ohashi, and M. Akiyma, J. Stat. Phys. **62**, 1121 (1991).

[50] S. Chen, D. Martinez, W. Matthaeus, and H. Chen, J. Stat. Phys. **68**, 533 (1992).

[51] B. Boghosian, J. Yepez, F. Alexander, and N. Margolus, Phys. Rev. E **55**, 4137 (1997).

[52] H. Chen, C. Teixeira, and K. Molvig, Int. J. Mod. Phys. C **8**, 675 (1997).

[53] P. Bhatnager, E. Gross, and M. Krook, Phys. Rev. **94**, 511 (1954).

[54] H. Chen, S. Chen, and W. Matthaeus, Phys. Rev. A **45**, 5339 (1992).

[55] S. Hou, Q. Zou, S. Chen, G. Doolen, and A. Cogley, J. Comp. Phys. **118**, 329 (1995).

[56] W. Miller, Phys. Rev. E **51**, 3659 (1995).

[57] Y.H. Qian, S. Succi, S.A. Orszag, Annu. Rev. Comp. Phys. **3**, 195 (1992).

[58] C. Aidun, and Y. Lu, J. Stat. Phys. **81**, 49 (1995).

[59] P. Skordos, Phys. Rev. E **48**, 4823 (1993).

[60] X. Shan, and H. Chen, Phys. Rev. E **47**, 1815 (1993).

[61] D. Grunau, S. Chen, and K. Eggert, Phys. Fluids **10**, 2557 (1993).

[62] A. Gunstensen, and D. Rothman, J. Geol. Res. **98**, 6431 (1993).

[63] E. Flekkøy, T. Rage, U. Oxaal, and J. Feder, Phys. Rev. Lett. **77**, 4170 (1996).

[64] A. Ladd, Phys. Rev. Lett. **76**, 1392 (1996).

[65] O. Behrend, Phys. Rev. E **52**, 1164 (1995).

[66] C. Aidun, Y. Lu, and E.-J. Ding, preprint, (1997).

[67] P. Raiskinmäki, A. Koponen, M. Kataja, and J. Timonen, to be published.

[68] F. Alexander, S. Chen, and J. Sterling, Phys. Rev. E **47**, R2249 (1993).

[69] Y. Chen, H. Ohashi, and M. Akiyma, J. Stat. Phys. **81**, 71 (1995).

[70] G. McNamara, A. Garcia, and B. Alder, J. Stat. Phys. **81**, 395 (1995).

[71] J. Kaandorp, C. Lowe, D. Frenkel, and P. Sloot, Phys. Rev. Lett. **77**, 2328 (1996).

[72] S. Hou, J. Sterling, S. Chen, and G. Doolen, Fields Institute Communications **6**, 151 (1996).

[73] F. Hayot, and L. Wagner, Europhys. Lett. **33**, 435 (1996).

[74] S. Chen, H. Chen, D. Martinez, and W. Matthaeus, Phys. Rev. Lett. **67**, 3776 (1991).

[75] S. Chen, S. Dawson, G. Doolen, D. Janecky, and A. Lawniczak, Computers Chem. Engng **19**, 617 (1995).

[76] E. Aharonov, and D. H. Rothman, Geophys. Res. Lett. **20**, 679 (1993).

[77] F. Nannelli, and S. Succi, J. Stat. Phys. **68**, 401 (1992).

[78] X. He, and G. Doolen, Phys. Rev. E **56**, 434 (1997).

[79] X. He, and L. Luo, Phys. Rev. E **55**, R6333 (1997).

[80] D. Noble, J. Georgiadis, and R. Buckius, J. Stat. Phys. **81**, 17 (1995).

[81] R. Maier, R. Bernard, and D. Grunau, Phys. Fluids **8**, 1788 (1996).

[82] D. Noble, S. Chen, J. Georgiadis, and R. Buckius, Phys. Fluids **7**, 203 (1995).

[83] R. Cornubert, D. d'Humiéres, and D. Levermore, Physica D **47**, 241 (1991).

[84] P. Lavallée, J. Boon, and A. Noullez, Physica D **47**, 233 (1991).

[85] M. Gallivan, D. Noble, J. Georgiadis, and R. Bockius, Int. J. Numer. Meth. Fluids **25**, 249 (1997).

[86] X. He, Q. Zou, L. Luo, M. Dembo, Journal of Stat. Phys. **129**, 357 (1996).

[87] O. Filippova, and D. Haenel, Computers in Fluids **26**, 697 (1997).

[88] D. Rothman, Geophys. **53**, 509 (1988).

[89] J. Berryman, and S. Blair, J. Appl. Phys. **60**, 1930 (1986).

[90] A. Ladd, private communication.

[91] G. A. Kohring, Physica A **186**, 97 (1992).

[92] J. F. McCarthy, Phys. Fluids **6**, 435 (1994).

[93] I. Ginzbourg, and D. d'Humierés, J. Stat. Phys. **84**, 927 (1996).

[94] S. Succi, private communication.

[95] D. Kandhai, D. Vidal, A. Hoekstra, H. Hoefsloot, P. Iedema, and P. Sloot, to be published.

[96] D. d'Humiéres, and P. Lallemand, Physica A **140**, 326 (1986).

[97] L.P. Kadanoff, G. R. McNamara, and G. Zanetti, Complex Systems **1**, 791 (1987).

[98] A. Jäsberg, A. Koponen, M. Kataja, and J. Timonen, to be published.

[99] P. Pachero, *Parallel programming with MPI* (Morgan Kaufman publishers, 1997).

[100] G. Fox, R. Williams, and P. Messina, *Parallel computing works!* (Morgan Kaufman Publishers, 1994).

[101] G. Punzo, F. Massaioli, and S. Succi, Computers in physics **8**, 705 (1994).

[102] P. Skordos, Parallel simulation of subsonic fluid dynamics on a cluster of workstations, in *Proceedings of high performance distributed computing 95* (number 4th IEEE international symposium, august 1995).

[103] K. Balasubmanian, F. Hayot, and W. Saam, Phys. Rev. A **36**, 2248 (1987).

[104] S. Succi, E. Foti, and F. Higuera, Europhys. Lett. **10**, 433 (1989).

[105] M. Sahimi, and D. Stauffer, Chem. Engng Sci. **46**, 2255 (1991).

[106] S. Chen, G. Doolen, and W. Matthaeus, J. Stat. Phys. **64**, 1133 (1991).

[107] U. Brosa, and D. Stauffer, J. Stat. Phys. **63**, 405 (1991).

[108] A. Cancelliere, C. Chang, E. Foti, D. Rothman, and S. Succi, Phys. Fluids A **2**, 2085 (1990).

[109] S. Chen, K. Diemer, G. Doolen, K. Eggert, C. Fu, S. Gutman, and B. Travis, Physica D **47**, 72 (1991).

[110] A. Heijs, and C. Lowe, Phys. Rev. E **51**, 4346 (1995).

[111] F. A. L. Dullien, *Porous Media. Fluid Transport and Pore Structure* (Academic Press, San Diego, 1979).

[112] P. M. Adler, *Porous media. Geometry and Transports* (Butterworth-Heinemann, Boston, 1992).

[113] G. E. Pike, and C. H. Seager, Phys. Rev. B **10**, 1421 (1974).

[114] C. K. Ghaddar, Phys. Fluids **7**, 2563 (1995).

[115] I. L. Clayes, and J. F. Brady, J. Fluid. Mech. **251**, 443 (1993).

[116] J. J. L. Higdon, and G. D. Ford, J. Fluid. Mech. **308**, 341 (1996).

[117] D. Clague, and R. Phillips, Phys. Fluids **9**, 1562 (1997).

[118] K. Niskanen, and M. Alava, Phys. Rev. Lett. **73**, 3475 (1994).

List of publications

I Permeability of three-dimensional random fibre webs

A. Koponen, D. Kandhai, E. Hellén, M. Alava, A. Hoekstra, M. Kataja, K. Niskanen, P. Sloot, and J. Timonen

Phys. Rev. Lett. **80**, 716 (1998).
https://doi.org/10.1103/PhysRevLett.80.716
The simulations were performed by A. Koponen and D. Kandhai. The paper was mainly written by A. Koponen.

II Tortuous flow in porous media

A. Koponen, M. Kataja, and J. Timonen

Phys. Rev. E **54**, 406 (1996).
https://doi.org/10.1103/PhysRevE.54.406
The simulations were performed by A. Koponen. The paper was mainly written by A. Koponen.

III Permeability and effective porosity of porous media

A. Koponen, M. Kataja, and J. Timonen

Phys. Rev. E **56**, 3319 (1997).
https://doi.org/10.1103/PhysRevE.56.3319
The simulations were performed by A. Koponen. The paper was mainly written by A. Koponen.

IV Lattice-Boltzmann hydrodynamics on parallel systems

D. Kandhai, A. Koponen, A. Hoekstra, M. Kataja, J. Timonen, and P. Sloot

Accepted for publication in Comput. Phys. Commun.
https://doi.org/10.1016/S0010-4655(98)00025-3
The simulations were performed by D. Kandhai and A. Koponen. The paper was mainly written by D. Kandhai.

V Implementation aspect of 3D lattice-BGK: boundaries, accuracy, and a new fast relaxation method

D. Kandhai, A. Koponen, A. Hoekstra, M. Kataja, J. Timonen, and P. Sloot

Submitted to J. Comp. Phys.
https://doi.org/10.1006/jcph.1999.6191

The simulations were performed by D. Kandhai and A. Koponen. A. Koponen wrote the sections on the body force, checkerboarding and IMR-method.